

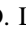
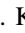

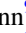








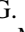
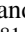




The Optical Two- and Three-dimensional Fundamental Plane Correlations for Nearly 180 Gamma-Ray Burst Afterglows with Swift/UVOT, RATIR, and the Subaru Telescope

M. G. Dainotti^{1,2,3,4} , S. Young⁵ , L. Li⁶ , D. Levine⁷ , K. K. Kalinowski⁸ , D. A. Kann⁹ , B. Tran¹⁰,
L. Zambrano-Tapia¹¹, A. Zambrano-Tapia¹¹, S. B. Cenko^{12,13}, M. Fuentes¹¹, E. G. Sánchez-Vázquez¹⁴, S. R. Oates¹⁵ ,
N. Fraija¹⁶ , R. L. Becerra¹⁷ , A. M. Watson¹⁶ , N. R. Butler¹⁸ , J. J. González¹⁶ , A. S. Kutyrév^{7,19}, W. H. Lee¹⁶,
J. X. Prochaska²⁰ , E. Ramirez-Ruiz²¹ , M. G. Richer²² , and S. Zola²³ 

¹ Division of Science, National Astronomical Observatory of Japan, 2-21-1 Osawa, Mitaka, Tokyo 181-8588, Japan; maria.dainotti@nao.ac.jp

² The Graduate University for Advanced Studies (SOKENDAI), 2-21-1 Osawa, Mitaka, Tokyo 181-8588, Japan

³ Space Science Institute, 4750 Walnut Street, Boulder, CO 80301, USA

⁴ SLAC National Accelerator Laboratory, 2575 Sand Hill Road, Menlo Park, CA 94025, USA

⁵ Department of Physics and Astronomy, University of Pennsylvania, 209 South 33rd Street, Philadelphia, PA 19104, USA

⁶ ICRA Net, Piazza della Repubblica 10, I-65122 Pescara, Italy; liang.li@icranet.org

⁷ Department of Astronomy, University of Maryland, College Park, MD 20742-4111, USA

⁸ Wydział Fizyki, Astronomii i Informatyki Stosowanej, Uniwersytet Jagielloński, ul. Łojasiewicza 11, 30-348 Kraków, Poland

⁹ Instituto de Astrofísica de Andalucía (IAA-CSIC), Glorieta de la Astronomía s/n, E-18008 Granada, Spain

¹⁰ Centennial High School, 1820 Rimpau Avenue, Corona, CA 92881, USA

¹¹ Scientific Caribbean Foundation, 12 Camino Francisco Rivera, San Juan, PR 00926, USA

¹² Astrophysics Science Division, NASA Goddard Space Flight Center, MC 661, Greenbelt, MD 20771, USA

¹³ Space Science Institute, 4765 Walnut Street, Boulder, CO 80301, USA

¹⁴ Latino Education Advancement Foundation, 210 East Lexington Street, Baltimore MD 21202, USA

¹⁵ School of Physics and Astronomy, University of Birmingham, Birmingham B15 2TT, UK

¹⁶ Instituto de Astronomía, Universidad Nacional Autónoma de México, Apartado Postal 70-264, 04510 México, CDMX, Mexico

¹⁷ Instituto de Ciencias Nucleares, Universidad Nacional Autónoma de México, Apartado Postal 70-264, 04510 México, CDMX, Mexico

¹⁸ School of Earth and Space Exploration, Arizona State University, Tempe, AZ 85287, USA

¹⁹ Astrophysics Science Division, NASA Goddard Space Flight Center, 8800 Greenbelt Road, Greenbelt, MD 20771, USA

²⁰ Department of Astronomy and Astrophysics, UCO/Lick Observatory, University of California, Santa Cruz, 1156 High Street, Santa Cruz, CA 95064, USA

²¹ Department of Astronomy, University of California, Berkeley, CA 94720-3411, USA

²² Instituto de Astronomía, Universidad Nacional Autónoma de México, Unidad Académica en Ensenada, 22860 Ensenada, BC, Mexico

²³ Astronomical Observatory, Jagiellonian University, ul. Orla 271, 30-244 Kraków, Poland

Received 2021 September 21; revised 2022 June 3; accepted 2022 June 3; published 2022 July 21

Abstract

Gamma-ray bursts (GRBs) are fascinating events due to their panchromatic nature. We study optical plateaus in GRB afterglows via an extended search into archival data. We comprehensively analyze all published GRBs with known redshifts and optical plateaus observed by many ground-based telescopes (e.g., Subaru Telescope, RATIR) around the world and several space-based observatories such as the Neil Gehrels Swift Observatory. We fit 500 optical light curves, showing the existence of the plateau in 179 cases. This sample is 75% larger than the previous one, and it is the largest compilation so far of optical plateaus. We discover the 3D fundamental plane relation at optical wavelengths using this sample. This correlation is between the rest-frame time at the end of the plateau emission, T_{opt}^* , its optical luminosity, L_{opt} , and the peak in the optical prompt emission, $L_{\text{peak,opt}}$, thus resembling the three-dimensional (3D) X-ray fundamental plane (the so-called 3D Dainotti relation). We correct our sample for redshift evolution and selection effects, discovering that this correlation is indeed intrinsic to GRB physics. We investigate the rest-frame end-time distributions in X-rays and optical (T_{opt}^* , T_X^*), and conclude that the plateau is achromatic only when selection biases are not considered. We also investigate if the 3D optical correlation may be a new discriminant between optical GRB classes and find that there is no significant separation between the classes compared to the Gold sample plane after correcting for evolution.

Unified Astronomy Thesaurus concepts: [Gamma-ray bursts \(629\)](#)

Supporting material: machine-readable table

1. Introduction

Gamma-ray bursts (GRBs), among the most luminous phenomena in the universe, originate from the deaths of massive stars (Woosley 1993; Paczyński 1998; Woosley & Bloom 2006; Cano et al. 2017) or the merging of two compact objects, like neutron stars (NSs; Duncan & Thompson 1992; Usov 1992; Thompson 1994; Metzger et al. 2011) and black

holes (BHs; Narayan et al. 1992). These models can have hyperaccreting BHs or fast-spinning newly born highly magnetized NSs (magnetars) as central engines.

To distinguish between the different origins, we categorize GRBs according to their phenomenology. The GRB prompt emission is observed from hard X-rays to ≥ 100 MeV γ -rays, and sometimes also in the optical (Blake et al. 2005; Vestrand et al. 2005; Beskin et al. 2010). The afterglow (e.g., Costa et al. 1997; van Paradijs et al. 1997; Piro et al. 1998; Gehrels et al. 2009; Wang et al. 2015) is the long-lasting multiwavelength emission (in X-rays, optical, and sometimes radio) following the prompt.



Original content from this work may be used under the terms of the [Creative Commons Attribution 4.0 licence](#). Any further distribution of this work must maintain attribution to the author(s) and the title of the work, journal citation and DOI.

GRBs are traditionally further classified as short (SGRBs) and long GRBs (LGRBs), depending on their duration: $T_{90} \leq 2$ s or $T_{90} \geq 2$ s,²⁴ respectively (Mazets et al. 1981; Kouveliotou et al. 1993). Zhang et al. (2009) proposed a classification based on the GRBs’ progenitors, according to which GRBs are divided in Type I/II; see Figure 8 in Zhang et al. (2009) and refer to Kann et al. (2011) for a discussion of controversial cases. Type II GRBs originate from the collapse of massive stars (Woosley 1993). These include LGRBs, X-ray flashes (XRFs) with soft spectra and greater fluence in X-rays (2–30 keV) than in γ -rays (30–400 keV; Heise et al. 2001), ultralong GRBs (ULGRBs) with $T_{90} > 1000$ s (Gendre et al. 2013; Levan et al. 2014; Piro et al. 2014; Greiner et al. 2015; Kann et al. 2018; Gendre et al. 2019), and GRBs associated with Type Ic supernovae (SNe Ic). GRB-SNe Ic are further classified in A, B, C, D, and E classes (Hjorth et al. 2003; Dainotti et al. 2007). The A, B, and C classes, which are more spectroscopically associated with SNe, are used in this work, hereafter denoted as GRB-SNe ABC. It is debated if all LGRBs should have an associated SN (Fynbo et al. 2006; Della Valle et al. 2006), because there have been cases such as GRB 060614 and GRB 060505 for which the SN should have been seen and since it was not, either the SN was at least two magnitudes smaller than the other associated SNe or simply was not seen. Due to these observational differences it was suggested (Fynbo et al. 2006; Della Valle et al. 2006) that those GRBs-SNe may form a new population different from the regular LGRBs for which the SNe is not observed. Thus, we also choose to keep separated in our analysis this class of events. Type I GRBs, resulting from the mergers of compact objects (Abbott et al. 2017a, 2017b), include SGRBs, SGRBs with extended emission (SEEs; Norris & Bonnell 2006; Levan et al. 2007; Norris et al. 2010; Dichiara et al. 2021; Rastinejad et al. 2022), and the intrinsically short (IS) GRBs, namely, short in the rest frame with $T_{90}^* = T_{90}/(1+z) < 2$ s (Levesque et al. 2010; Ahumada et al. 2021; Zhang et al. 2021; Rossi et al. 2022). Here, we use SGRBs, which include both SEEs and ISs as a unique class.

Observations of the X-ray afterglows performed by the Neil Gehrels Swift Observatory (Swift hereafter) revealed the presence of an X-ray plateau (O’Brien et al. 2006; Nousek et al. 2006; Zhang et al. 2006; Sakamoto et al. 2007; Evans et al. 2009). This phase generally lasts from 10^2 – 10^5 s and is followed by a power-law (PL) decay phase. The plateau can be explained with the long-lasting energy injection from the central engine by fallback mass accretion onto a BH (Kumar et al. 2008; Cannizzo & Gehrels 2009; Cannizzo et al. 2011) or with the energy injection produced by the spin-down luminosity of a highly magnetized millisecond newborn NS, a magnetar (e.g., Duncan & Thompson 1992; Usov 1992; Thompson 1994; Dai & Lu 1998; Zhang & Mészáros 2001; Troja et al. 2007; Dall’Osso et al. 2011; Metzger et al. 2011; Rowlinson et al. 2014; Rea et al. 2015; Li et al. 2018b; Stratta et al. 2018; Metzger 2019; Fraija et al. 2021). The plateau found in X-rays and optical has been identified as a trait that may standardize GRBs. Dainotti et al. (2016, 2017b), Dainotti & Del Vecchio (2017), and Li et al. (2018b) explored the luminosity at the end of the plateau, $L_{X,a}$ versus its rest-frame time $T_{X,a}^*$ (known as the Dainotti relation or 2D L–T relation), with the rest-frame time denoted with an asterisk. Rowlinson et al. (2014) showed that the Dainotti relation in X-rays is recovered within the magnetar scenario with

a slope for $L_a - T_{X,a}^*$ of -1 . Within the cosmological context, this correlation has already been applied to construct a GRB Hubble diagram out to $z > 8$ (Cardone et al. 2009, 2010; Postnikov et al. 2014; Dainotti et al. 2013).

As pointed out in Dainotti et al. (2008, 2010, 2016, 2017a, 2017b, 2018), to obtain a class of GRBs that can be well standardized, we need to select a GRB subsample with well-defined properties from a morphological or physical point of view. Thus, we segregate each class in GRBs-SNe Ic, XRFs, X-ray-rich (XRR; an intermediate case between the LGRBs and XRFs), ULGRBs, SGRBs, SEE, IS GRBs, and LGRBs. LGRBs are defined as the total sample from which we remove all other classes. Regarding the connection between prompt and plateau emission, we annotate the peak prompt luminosity in 1 s, $L_{X,\text{peak}}$ versus $T_{X,a}^*$ correlation. A theoretical interpretation of this correlation is within the standard fireball model and with the changing of the microphysical parameters (van Eerten 2014a, 2014b). An extension of the 2D L–T relation has been obtained by adding the peak prompt luminosity, $L_{X,\text{peak}}$, leading to the so-called Dainotti 3D relation (Dainotti et al. 2016, 2017b, 2020b). We enhance the previous definition of Gold GRBs from Dainotti et al. (2016) with new criteria: identifying the plateaus with fewer gaps in the data points and with less fluctuation in the fluxes. The criteria guarantee a tighter correlation involving the plateau emission to use it as a future cosmological tool and a theoretical model discriminator.

In this work, we investigate (1) the 3D Dainotti relation in the optical; (2) the 3D optical correlation as a discriminant between GRB classes; (3) the 2D optical correlation with our incremented sample size to determine if it can be a discriminant among classes; and (4) if with a larger sample and with the correction for selection biases, whether the plateau is an achromatic feature between X-rays and optical. All this analysis has been performed exploring three different types of fitting, to show that the reliability of the results is independent from the particular chosen fitting function.

In Section 2, we describe the sample. In Section 3, we detail the methodology showing how we corrected for Galactic and host-galaxy extinction and fitted our sample. In Section 4, we present the 2D and 3D optical Dainotti relations, also corrected for selection biases and redshift evolution. We compare our results with previous results in X-ray in Section 5, and we discuss our conclusions in Section 6.

2. Sample Selection

We analyzed 500 GRB optical afterglows with known redshifts, thus building the most comprehensive sample of optical light curves (LCs) to date by searching the literature for all GRBs detected between 1997 May and 2021 May by several satellites, e.g., the Swift Ultraviolet/Optical Telescope (UVOT), and ground-based telescopes/detectors, e.g., the Subaru Telescope, Gamma-ray Burst Optical/Near-IR Detector (GROND), Re-ionization and Transients InfraRed camera/telescope (RATIR), the MITSuME (Kotani et al. 2005), etc. In our final sample, the redshifts span from $z = 0.06$ to $z = 8.23$ and the LCs are taken from Kann et al. (2006, 2010, 2011, 2022a, 2022b, in preparation), Li et al. (2012, 2015, 2018a), Oates et al. (2009, 2012), Zaninoni et al. (2013), Si et al. (2018), the RATIR collaboration, the GCN Circular Archive (GCN),²⁵ the Swift Burst Analyzer (Evans et al. 2010), and

²⁴ T_{90} is the time over which a burst emits from 5% to 95% of its prompt emission total measured counts.

²⁵ <https://gcn.gsfc.nasa.gov/>

Table 1
Fitting Parameters for the Sample of 179 GRBs

GRB	Author	z	T_{90} (s)	Class	$\log Fa$ ($\text{erg cm}^{-2}\text{s}^{-1}$)	$\log Fa\text{Err}$ ($\text{erg cm}^{-2}\text{s}^{-1}$)	$\log Ta$ (s)	$\log Ta\text{Err}$ (s)	β (s)	βErr (s)	$\log L(Ta)$ (erg s^{-1})	$\log L(Ta)\text{Err}$ (erg s^{-1})
970508A	Kann[1], Kann[2]	0.83	13.2	XRF	-13.88	0.07	6.25	0.07	0.32	0.15	43.46	0.08
980326A	GCN[3]	1	5	L	-14.54	1.12	5.31	0.60	0.66	0.70	43.07	1.14
990510A	Kann[2]	1.62	67.58	L	-12.30	0.02	4.83	0.01	0.17	0.15	45.59	0.07
000301C	Si[4]	2.03	2	IS	-13.83	0.12	5.88	0.05	0.59	0.12	44.45	0.13
000926A	Kann[1]	2.07	25	L	-12.89	0.03	5.12	0.02	1.01	0.16	45.61	0.08
010222A	Li[5], Wata- nabe[6]	1.48	2	L	-12.61	0.02	4.64	0.02	0.76	0.22	45.44	0.09
011211A	Kann[2]	2.14	270	L	-13.52	0.06	5.23	0.04	0.41	0.15	44.72	0.10
020124A	GCN[7]	3.198	45.91	L	-12.77	0.05	4.45	0.07	1.32	0.25	46.38	0.17
021004A	Li[5]	2.34	100	L	-12.92	0.02	5.40	0.02	0.67	0.14	45.53	0.08
030226A	Kann[1]	1.99	22.09	L	-13.14	0.06	4.97	0.03	0.57	0.12	45.11	0.09
030328A	Kann[1]	1.52	199.2	L	-12.70	0.02	4.38	0.02	0.36	0.45	45.21	0.18
030329A	Si[4]	0.17	62.9	SN-A	-11.76	0.09	5.50	0.05	0.41	0.17	44.10	0.09
030429A	Li[5], Leven[8]	2.658	10.3	XRF	-14.08	0.82	5.46	0.28	0.22	0.24	44.25	0.83
040924A	Kann[1]	0.86	2.39	SN-C	-12.20	0.04	3.50	0.04	0.63	0.48	45.26	0.14
041006A	Si[4]	0.72	17.4	SN-C	-12.45	0.03	4.08	0.03	0.36	0.27	44.77	0.07
050319A	Zaninoni[9]	3.24	152.54	XRR	-12.83	0.02	4.44	0.03	0.74	0.42	45.98	0.26
050401A	Li[5], Kam- ble[10]	2.90	32.09	L	-13.60	0.12	4.14	0.16	0.39	0.05	44.89	0.12
050408A	Si[4]	1.24	34	L	-13.25	0.03	4.36	0.05	0.28	0.27	44.45	0.10
050416A	Li[5]	0.65	2.49	XRF- D- IS-SN	-13.54	0.05	4.15	0.06	0.92	0.30	43.70	0.08
050502A	GCN[11]	3.79	20	L	-12.60	0.04	3.72	0.03	0.76	0.16	46.37	0.12
050502B	GCN[12]	5.2	17.5	L	-12.45	0.12	3.58	0.14	0.90	0.06	46.93	0.13
050525A	Kann[2]	0.61	8.83	SN- B-XRR	-11.70	0.07	3.22	0.10	0.52	0.08	45.39	0.07
050603A	Kann[2]	2.82	21	L	-11.88	0.13	4.45	0.08	0.95	0.08	46.91	0.14
050730A	Kann[2]	3.97	156.5	L	-12.37	0.04	4.34	0.05	0.52	0.05	46.48	0.06
050801A	Kann[2]	1.38	19.4	XRR	-10.98	0.02	2.64	0.02	0.69	0.34	46.97	0.13
050802A	Kann[2]	1.71	30	L	-11.61	0.08	2.91	0.09	0.72	0.03	46.56	0.08
050820A	Kann[2], Zaninoni[9]	2.61	244.69	L	-11.97	0.01	4.46	0.02	0.72	0.03	46.62	0.02
050824A	Kann[2]	0.83	22.58	XRF- SN-E	-12.50	0.03	3.65	0.06	0.45	0.18	44.87	0.06
050904A	Li[5], Yost[13]	6.295	181.57	UL	-14.18	0.13	5.54	0.07	1.00	0.09	45.47	0.15
050908A	Zaninoni[9]	3.34	17.37	XRR	-12.61	0.08	3.26	0.13	1.80	0.09	46.90	0.10
050922C	Kann[2], Zaninoni[9]	2.2	4.54	IS	-11.65	0.01	3.77	0.01	0.56	0.01	46.69	0.01
051028A	Li[5], Castro- Tirado[15]	3.6	16	SN-B	-13.07	0.23	4.04	0.25	1.10	0.18	46.07	0.26
051109A	Zaninoni[9]	2.35	37.23	L	-12.14	0.03	3.74	0.04	0.96	0.04	46.47	0.04
051111A	Si[4]	1.55	59.78	L	-10.91	0.03	2.77	0.04	0.76	0.07	47.18	0.04
060124A	Zaninoni[9]	2.3	13.63	XRR	-11.66	0.03	3.63	0.04	0.73	0.08	46.81	0.05
060206A	Zaninoni[9]	4.05	7.59	XRR-IS	-12.01	0.00	4.29	0.00	0.77	0.01	47.03	0.01
060210A	Kann[2]	3.91	255	L	-12.45	0.04	3.24	0.04	0.99	0.03	46.70	0.04
060313A	Kann[16]	1.1	2	S	-12.89	0.13	3.58	0.39	0.85	0.06	44.88	0.13
060418A	Kann[2]	1.49	144	XRR	-10.43	0.02	2.58	0.02	0.69	0.11	47.59	0.05

Note. The columns show in order the name of the GRB, the GCN information, the redshift, the T_{90} , the GRB class, the log of the flux at the end of the plateau emission and its error, the time at the end of the plateau emission and its error, the spectral index of the plateau and its error, and the logarithm of the luminosity at the end of the plateau emission and its error. Errors are quoted at the 1σ level.

(This table is available in its entirety in machine-readable form.)

other literature. The GRB name, redshift, fitting parameters, and data source of a portion of our data sample are given in Table 1—the full table with our sample of 179 GRBs is available in machine-readable format. Following Dainotti et al. (2021a), we use 69 LCs from Kann et al. (2006, 2010, 2011, 2021a, 2022b, in preparation), 22 GRBs from Li et al.

(2012, 2015, 2018a, 2022, in preparation), 3 GRBs from Oates et al. (2009, 2012), 19 GRBs from Zaninoni et al. (2013), and 16 GRBs from Si et al. (2018), which were in turn taken from Li et al. (2012) and Kann et al. (2006). Out of those, we combined the LCs of 6 GRBs from different authors: 3 from Li et al. (2012, 2015), 1 from Kann et al. (2010) and

Zaninoni et al. (2013), and 1 from Kann et al. (2010), Zaninoni et al. (2013), and Oates et al. (2009, 2012). Additionally, we gathered 50 LCs from the GCN, Swift Burst Analyzer, the RATIR collaboration, and other literature.

We have also investigated GRB data points taken from the Subaru Telescope, updating previous LCs and improving the fits of the following 18 GRBs: 110422A, 140801A, 140423A, 141121A, 020124A, 110801A, 100513A, 110503A, 980326A, 150413A, 140907A, 180325A, 160131A, 151027A, 160227A, 151029A, 170113A, and 140206A.

3. Methodology

We briefly describe the analysis performed on LCs collected by Li et al. (2012, 2015, 2018a), Kann et al. (2006, 2010, 2011), Oates et al. (2012), Zaninoni et al. (2013), and Si et al. (2018), and the LCs taken from the GCN. A flow chart summarizing all the steps of the analysis can be found in Figure 1. All errors in this paper are quoted at the 1σ level.

3.1. Correction for Galactic and Host-galaxy Extinction

For the GRBs not already corrected for host extinction in the papers cited previously, we computed the extinction factor $10^{-A_\lambda/2.5}$ in flux density space. For the GRBs taken from Li et al. (2012, 2015, 2018a), we followed Li et al. (2012, 2015, 2018a) to correct for Galactic and host-galaxy extinction through the extinction parameter A_λ , assuming $R_v = 3.1$ and the Small Magellanic Cloud (SMC), Milky Way (MW), or Large Magellanic Cloud (LMC) dust models. The flux contribution coming from the host galaxy at very late times ($\sim 10^6$ s after the GRB trigger) for some GRBs has also been subtracted.

For the GRBs taken from Kann et al. (2006, 2019) we follow Kann et al. (2006, 2019). More specifically, for each afterglow, the multiband LCs are fit with a single PL, a smoothly broken PL, or a series of these. If necessary, a constant host-galaxy component is added, and a special supernova-model fit is applied if such an SN is detected (see Kann et al. 2019). The LCs are corrected for Galactic extinction, and the spectral energy distribution (SED) is assumed to be constant over the region fit and analyzed to determine the line-of-sight extinction from the host galaxy. The SED is then used twofold: first, it allows us (after necessary host- and SN-component removal) to shift other bands to the R_C band, for which there are essentially always measurements, creating a compound LC with maximized data density and temporal coverage. The LCs gathered by Oates et al. (2009, 2012) are corrected for host extinction using the same values as Oates et al. (2012). In Oates et al. (2009), for each GRB, the onset of the prompt γ -ray emission (the start time of the T_{90} parameter) is equal to the start time of the UVOT LC. However, here we convert it using the Swift Burst Alert Telescope (BAT) trigger time as the start time of the UVOT LCs to have a consistent BAT trigger time, as the other LCs in the sample.

For the LCs gathered from Zaninoni et al. (2013), SEDs are created at early and late times for each GRB, using optical filters for which data were available; spectral index values β_{opt} are derived from fitting these SEDs, corrected for host and Galactic extinction.

For the 50 GRBs gathered from GCNs, we correct for Galactic extinction using the reddening maps from Schlegel et al. (1998), and the $A_b/E(B - V)_{\text{SFD}}$ values from

Schlafly & Finkbeiner (2011). For Swift UVOT bandpasses, $A_b/E(B - V)_{\text{SFD}}$ values are taken from the York Extinction Solver (McCall 2004).

3.2. Magnitude Conversions

We converted magnitudes across 18 bandpasses ($B, H, I, I_C, J, K, K_S, R, R_C, V, Z, b, g, i, r, u, v,$ and z) into energy fluxes ($\text{erg cm}^{-2} \text{s}^{-1}$) to the R band using a conversion of zero-point flux densities in any given band. We take the optical spectral indices from the literature; when no value has been found, we assume a constant photon index extrapolated from X-ray and taken from Evans et al. (2009) or GCNs. The formulation for the conversion of flux densities to the R band is the following:

$$f_R = f_X \left(\frac{\lambda_X}{\lambda_R} \right)^{-\beta} \quad (1)$$

Then, we use the following equation to convert from magnitude to flux:

$$F_R = \nu_R f_X \left(\frac{\lambda_X}{\lambda_R} \right)^{-\beta} 10^{-m_X/2.5}, \quad (2)$$

where, given a band X , λ_X is the effective wavelength (\AA), f_X is the zero-point flux density ($\text{erg cm}^{-2} \text{s}^{-1} \text{Hz}^{-1}$), ν_R is the effective frequency (Hz) of the R band in the Johnson–Cousins system, m_X is the observed magnitude, and β is the optical spectral index either taken from the literature or taken as $\Gamma - 1$, where Γ is the photon index in X-ray extrapolated from Evans et al. (2009) or GCNs. We take effective wavelengths from Bessell et al. (1998) for Johnson–Cousins bands, Fukugita et al. (1996) for SDSS bands, Poole et al. (2008) for Swift UVOT bands. Photon index values were taken from GCNs in cases in which the Swift XRT website did not have a photon index for a particular GRB.

Examples of two LCs show data across six bandpasses (top left panel of Figure 2) and an enhanced coverage with data from the Subaru Telescope (top right panel of Figure 2).

3.3. Light-curve Fitting with the Willingale et al. (2007) Model

We confirm the existence of a plateau by fitting the LCs to the phenomenological Willingale et al. (2007, hereafter W07) model (see the dashed black and solid red lines in Figure 2).²⁶ We include all 179 GRBs that can be successfully fitted by the W07 model:

$$f(t) = \begin{cases} F_i \exp\left(\alpha_i \left(1 - \frac{t}{T_i}\right)\right) \exp\left(-\frac{t_i}{t}\right) & \text{for } t < T_i \\ F_i \left(\frac{t}{T_i}\right)^{-\alpha_i} \exp\left(-\frac{t_i}{t}\right) & \text{for } t \geq T_i, \end{cases} \quad (3)$$

where the prompt (index “ $i = p$ ”) and the afterglow (“ $i = a$ ”) could be modeled, in principle. The LC $f_{\text{tot}}(t) = f_p(t) + f_a(t)$ contains two sets of four free parameters ($T_i, F_i, \alpha_i,$ and t_i), where T_i and F_i are the end times and corresponding fluxes at the plateau end, α_i is the temporal PL decay index, and t_i is the initial rise timescale, usually fixed at zero. We exclude cases when the afterglow fitting procedure fails or the determination

²⁶ The W07 model makes no assumptions on the underlying physics.

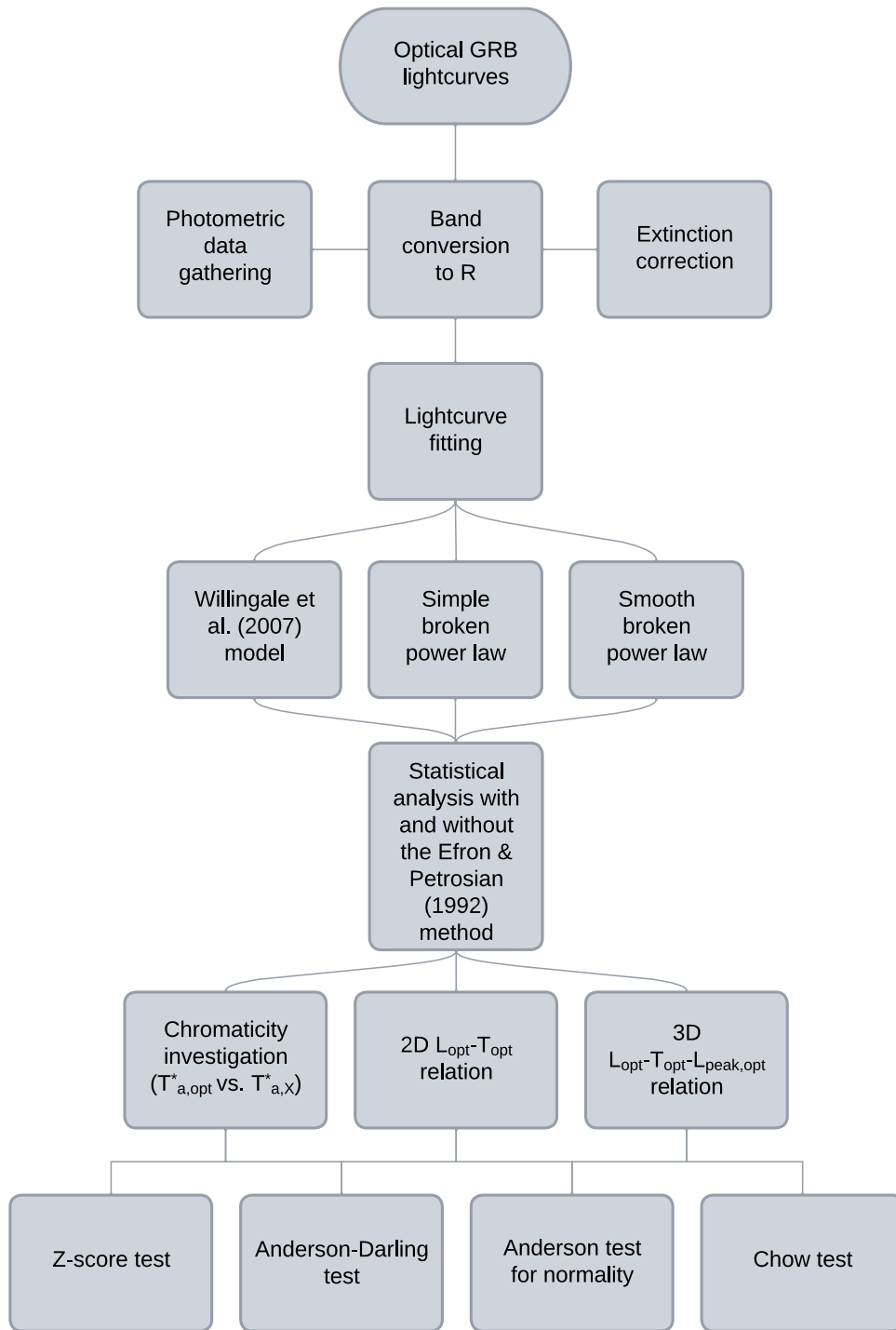


Figure 1. Flow chart summarizing all the steps of the analysis.

of 1σ confidence intervals does not satisfy the Avni (1976) χ^2 rules. We show in the middle panels of Figure 2 two examples of LCs fitted with the W07 model from a GRB that shows the peak of the prompt emission indicated by an empty black circle. Of the 500 LCs fitted, 179 yield a good fitting. We reject 69 for being a PL, 42 for not fulfilling the aforementioned $\Delta\chi^2$ prescriptions, 43 for being too scattered, 148 for having insufficient data points, and 19 when multiple reasons above are happening at the same time. We clarify here that the fit shows the presence of the plateau emission, given by several

models such as the W07, smoothly broken power law (BPL), or simple BPL. For the successfully fitted LCs, we compute the source rest-frame isotropic luminosity L_{opt} (erg s $^{-1}$) at the end of the plateau emission and, when possible, the peak prompt luminosity $L_{\text{peak,opt}}$ (erg s $^{-1}$) following Dainotti et al. (2016, 2017a, 2017b, 2020b, 2021a). The luminosities are defined as follows:

$$L_{\text{opt}} = 4\pi D_L^2(z) F_{\text{opt}} K, \quad L_{\text{peak,opt}} = 4\pi D_L^2(z) F_{\text{peak,opt}} K, \quad (4)$$

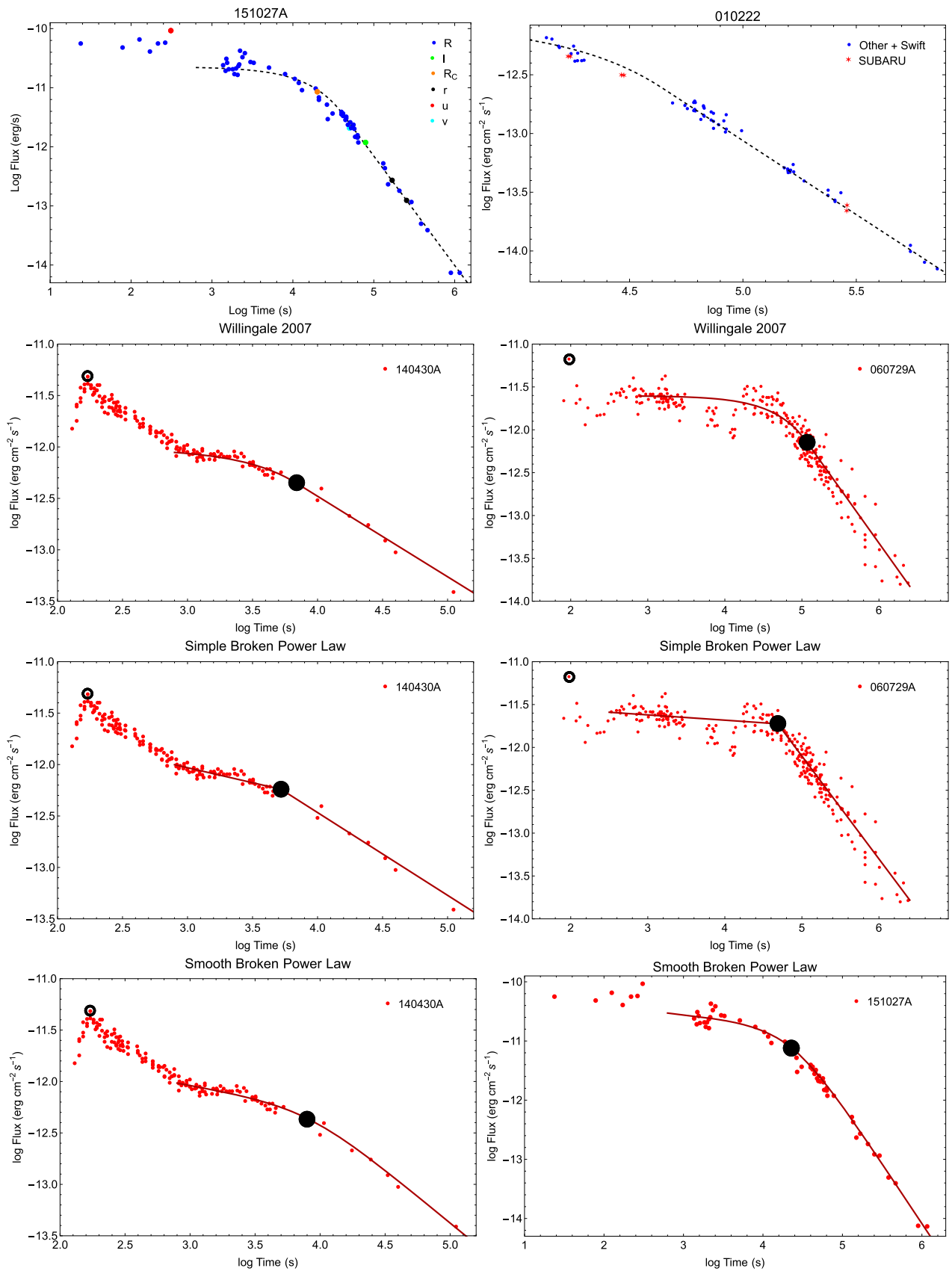


Figure 2. The top left panel shows an LC with multiple bands and the upper right panel shows an LC including the Subaru data with the W07 function superimposed. The second row of panels show examples of LCs that present a peak of the prompt emission, indicated by an empty black circle and the end of the plateau emission with a filled black circle with the W07 function superimposed with a dark red curve. The third and fourth rows of panels show the same, but with simple and smoothly BPL, respectively.

where $D_L(z)$ is the luminosity distance assuming a flat Λ CDM cosmological model with $\Omega_M = 0.3$ and $H_0 = 70 \text{ km s}^{-1} \text{ Mpc}^{-1}$, and F_{opt} and $F_{\text{peak,opt}}$ are the measured optical energy flux ($\text{erg cm}^{-2} \text{ s}^{-1}$) at time T_{opt} , the end of the plateau, and in the peak of the prompt emission over a 1 s interval, respectively. Following Bloom et al. (2001), we apply the K -correction $K = 1/(1+z)^{1-\beta_{\text{opt}}}$, where β is the optical spectral index.²⁷ We use the same β_{opt} for all LCs assuming no spectral evolution. Finally, we construct a subsample from the 179 GRBs called the new Gold sample via the morphology conditions:

1. The plateau should not be too steep, with an angle of $<41^\circ$. The angle of the plateau is defined as $\tan^{-1}(\Delta F/\Delta T)$, with $\Delta F/\Delta T = (F_i - F_a)/(T_i - T_{\text{opt}})$, where i denotes the time at the beginning of the plateau.
2. The largest change between times in the first five consecutive points in the plateau, normalized to the length of the plateau, should be $(\Delta T/(T_{\text{opt}} - T_i))_{\text{max}} < 0.10$.
3. The largest relative change in flux in the first five consecutive points in the plateau should be $\Delta F_{\text{max}}/F < 0.10$.

The definition of the 41° comes from Dainotti et al. (2016) in which a Gaussian distribution characterizes the angular distribution; the angles $>41^\circ$ are the outliers beyond 1σ from that Gaussian. We show the plot of the Gaussian distribution for the X-ray data in Appendix B (Figure 10) of Dainotti et al. (2017a). To be consistent with the X-ray sample, we use the same definition.

This data quality criterion defines the new Gold sample, which includes 12 GRBs in the W07 fitting (42% larger than the previous sample of 7). These criteria are chosen such that the definition of the plateau is enhanced, allowing a minimal variation in flux and time while still preserving the existence of the sample; more restrictive criteria would have caused the sample to be smaller, less restrictive criteria would enlarge the sample, but allow larger variation in fluxes and larger gaps in time. Although these criteria may not be the only choices, they safely allow the Gold sample to be reconstructed following these specific criteria. The results of the fitting are provided in Table 2.

3.4. Light-curve Fitting with the Simple Broken Power-law and Smoothly Broken Power-law Models

To give generality to the analysis and to use a model that is not phenomenological and is driven by the underlying physics of the standard fireball model, we have also attempted to fit the sample of 179 with the simple and smoothly BPL. Specifically, the simple BPL reads as follows:

$$f(t) = \begin{cases} F_i \left(\frac{t}{T_i}\right)^{-\alpha_1} & \text{for } t < T_i \\ F_i \left(\frac{t}{T_i}\right)^{-\alpha_2} & \text{for } t \geq T_i, \end{cases} \quad (5)$$

where T_i is the time at the end of the plateau, and α_1 and α_2 are the slopes of the LC before and after the time T_i . Within this

analysis, we consider the cases that have the angle of the plateau $<41^\circ$ corresponding to $\alpha_1 < 0.8$, and we removed the cases in which $\sigma_{\alpha_2}/\alpha_2 < 1$ and $\sigma F/F < 1$ and σ_T/T . We denote with σ the error in 1σ . It is important to clarify here that we did not adopt the condition of the ratio of the α_1 error to the best-fit value $\sigma_{\alpha_1}/\alpha_1 < 1$ in approving fits because this would naturally introduce a bias against very flat plateaus. Indeed, if a plateau is very close to zero, a small error bar can be larger than 100%, but the plateau is still flat. To guarantee that the error bars still preserve the condition of flatness, we instead use a criterion in which $\sigma_{\alpha_1} < 0.8$. From the analysis of the 179 LCs, we obtain 99 cases that fulfill these and the χ^2 requirements.

We also attempt to fit the sample of 179 GRBs with the smoothly BPL:

$$f(t) = F_i \left(\left(\frac{t}{T_i} \right)^{S\alpha_1} + \left(\frac{t}{T_i} \right)^{S\alpha_2} \right)^{-\frac{1}{S}}, \quad (6)$$

with all parameters defined as before but with the addition of a smoothing parameter S . After the smoothly BPL fitting we are left with 45 GRBs that fulfill the χ^2 requirements. We present the results of the simple and smoothly BPL fittings in Tables 3 and 4. Two examples of fitting with the simple and smoothly BPL models are shown in the bottom panel of Figure 2. As expected, both the end time of the plateau and its corresponding fluxes are compatible within 1σ .

4. The Optical Correlations

We present the results of the fitting with and without evolution for the 2D and 3D correlations using the W07 and the two BPL models. We show the z -score values for all three models calculated as the distance from the Gold fundamental plane to the other classes (see Tables 2, 3, and 4). In all plots, all the logarithmic scales are in the base of 10.

4.1. The 3D Fundamental Plane Relation with the Willingale et al. (2007) Model: $L_{\text{opt}}^{(\cdot)} T_{\text{opt}}^{(*,\cdot)} - L_{\text{peak,opt}}^{(\cdot)}$

We find that 58 out of the total sample of 179 GRBs show a peak in the prompt emission. To determine the peak flux in these cases, we consider the highest flux before the initial decay phase and when the time is nearly coincident with the peak flux in the X-ray data. Two examples of optical peak fluxes are shown in the bottom panels of Figure 2. With this information, we build the 3D optical correlation.

The optical fundamental plane relation is defined as

$$\log L_{\text{opt}} = C_0 + a \times \log T_{\text{opt}}^* + b \times \log L_{\text{peak,opt}}, \quad (7)$$

where C_0 is the normalization, a_{opt} and b_{opt} are the best-fit parameters related to $\log T_{\text{opt}}^*$ and $\log L_{\text{peak,opt}}$, respectively, see the top left panel of Figure 3. We also consider the evolutionary effects, and we correct for them following Efron & Petrosian (1992). The fundamental plane corrected for selection biases and redshift evolution is

$$\log L'_{\text{opt}} = C'_0 + a' \times \log T'_{\text{opt}} + b' \times \log L'_{\text{peak,opt}}, \quad (8)$$

where C'_0 , a' , and b' are the parameters of the plane corrected for selection biases (top right panel of Figure 3). The new variables are $L'_{\text{opt}} = L_{\text{opt}}/(1+z)^{k_{\text{opt,L}}}$, $L'_{\text{peak,opt}} = L_{\text{peak,opt}}/(1+z)^{k_{\text{opt,peak}}}$, and $T'_{\text{opt}} = T_{\text{opt}}/(1+z)^{k_{\text{opt,T}}}$ where $k_{\text{opt,L}} = 3.96 \pm 0.43$,

²⁷ When β_{opt} is not available, we use the XRT index.

Table 2
The Best-fit Parameters of the 2D and 3D Correlations with the W07 Model

Best-fit Parameters for the Subsamples in 2D with the W07 Model												
Class	N	Uncorrected for Evolution					Corrected for Evolution					
		a_{opt}	C_0	σ_{int}^2	z	Chow	a'_{opt}	C'_0	σ'^2_{int}	z'	Chow	$\Delta\sigma^2_{\text{int}}$
All GRBs	179	-0.91 ± 0.06	49.03 ± 0.23	0.73 ± 0.04	-1.65	0.87	-0.71 ± 0.06	47.27 ± 0.26	0.58 ± 0.03	-0.95	0.92	-20%
Gold	12	-0.85 ± 0.21	48.69 ± 0.76	0.54 ± 0.14	...	1.00	-0.66 ± 0.17	46.95 ± 0.78	0.34 ± 0.10	...	1.00	-37%
LGRBs	102	-0.84 ± 0.08	48.87 ± 0.31	0.70 ± 0.05	-2.39	0.69	-0.68 ± 0.07	47.18 ± 0.34	0.60 ± 0.05	-1.75	0.42	-14%
SGRBs	13	-0.79 ± 0.35	48.26 ± 1.37	1.32 ± 0.36	0.76	0.84	-0.55 ± 0.25	45.92 ± 1.22	0.91 ± 0.25	2.17	0.67	-31%
GRB-SNe Ic	26	-0.79 ± 0.09	47.93 ± 0.39	0.52 ± 0.07	5.23	0.05	-0.65 ± 0.12	46.83 ± 0.57	0.54 ± 0.09	1.41	0.54	$+3\%$
GRB-SNe ABC	19	-0.86 ± 0.10	48.33 ± 0.43	0.45 ± 0.08	4.34	0.16	-0.71 ± 0.11	47.23 ± 0.55	0.44 ± 0.10	0.26	0.63	$+0\%$
ULGRBs	7	-1.31 ± 0.45	50.77 ± 2.19	1.00 ± 0.45	0.54	0.74	-1.20 ± 0.34	49.74 ± 1.90	0.72 ± 0.34	0.80	0.49	-28%
XRFs	16	-1.04 ± 0.16	49.02 ± 0.66	0.70 ± 0.15	2.75	0.22	-0.69 ± 0.15	46.76 ± 0.70	0.49 ± 0.12	2.92	0.18	-30%
XRRs	44	-1.07 ± 0.12	49.67 ± 0.41	0.69 ± 0.08	-1.91	0.48	-0.85 ± 0.11	47.89 ± 0.46	0.49 ± 0.06	-1.39	0.58	-28%
Type I GRBs	13	-0.79 ± 0.35	48.26 ± 1.37	1.32 ± 0.36	0.76	0.84	-0.55 ± 0.25	45.92 ± 1.22	0.91 ± 0.25	2.17	0.67	-31%
Type II GRBs	171	-0.93 ± 0.06	49.12 ± 0.21	0.72 ± 0.04	-1.86	0.81	-0.73 ± 0.05	47.38 ± 0.23	0.56 ± 0.03	-1.39	0.86	-21%

Best-fit Parameters for the Subsamples in 3D with the W07 Model												
Class	N	Uncorrected for Evolution					Corrected for Evolution					
		a_{opt}	b_{opt}	C_0	σ_{int}^2	z	a'_{opt}	b'_{opt}	C'_0	σ'^2_{int}	z	$\Delta\sigma'^2_{\text{int}}$
All GRBs	58	-0.87 ± 0.09	0.48 ± 0.07	26.57 ± 3.44	0.44 ± 0.12	-0.97	-0.82 ± 0.10	0.34 ± 0.08	32.30 ± 3.94	0.37 ± 0.10	-0.94	-16%
Gold	6	-1.02 ± 0.39	0.38 ± 0.22	31.37 ± 10.19	0.60 ± 0.36	0.0	-0.96 ± 0.40	0.31 ± 0.26	34.18 ± 11.03	0.43 ± 0.35	0.0	-28%
LGRBs	31	-0.93 ± 0.13	0.49 ± 0.10	25.99 ± 4.79	0.47 ± 0.13	-0.98	-0.92 ± 0.13	0.45 ± 0.11	27.58 ± 5.30	0.34 ± 0.13	-0.94	-27%
GRB-SNe Ic	9	-0.69 ± 0.24	0.20 ± 0.16	38.33 ± 7.46	0.48 ± 0.21	0.20	-0.66 ± 0.22	0.23 ± 0.16	36.71 ± 7.60	0.46 ± 0.21	-0.27	-4%
GRB-SNe ABC	7	-0.81 ± 0.29	0.26 ± 0.18	35.86 ± 8.67	0.52 ± 0.26	0.19	-0.78 ± 0.25	0.30 ± 0.17	33.76 ± 8.20	0.47 ± 0.26	-0.26	-9%
XRFs	4	-0.94 ± 0.67	0.65 ± 0.28	18.62 ± 14.27	0.66 ± 0.45	-0.02	-1.34 ± 1.24	0.55 ± 0.29	24.87 ± 13.74	0.62 ± 0.51	0.10	-6%
XRRs	19	-0.77 ± 0.17	0.42 ± 0.18	28.75 ± 8.90	0.48 ± 0.15	-1.04	-0.65 ± 0.14	0.19 ± 0.13	38.65 ± 6.10	0.30 ± 0.11	-0.94	-36%

Note. The first vertical half of the table (left) shows the GRB classes, the normalization, the slope with their respective errors, and the intrinsic scatter σ_{int}^2 for each class for the 2D correlation uncorrected for selection biases. The second vertical half of the table (right) show the same variables, but corrected for selection biases (denoted by '). The final column (13) shows the fractional change in σ_{int}^2 among the classes after correcting for redshift evolution and selection biases. In the 2D subtable, columns (6) and (7) (columns (11) and (12)) show the z -score and Chow test p -value, representing two statistical tests comparing subclasses with the Gold fundamental plane without (with) the correction for redshift evolution. Similarly, z -scores for the 3D case are found in columns (7) and (12) of the lower subtable

Table 3
The Best-fit Parameters of the 2D and 3D Correlations with the Simple BPL Model

Best-fit Parameters for the Subsamples in 2D with the Simple BPL Model												
Class	N	Uncorrected for Evolution					Corrected for Evolution					$\Delta\sigma_{\text{int}}^{\prime 2}$
		a_{opt}	C_0	σ_{int}^2	z	Chow	a'_{opt}	C'_0	$\sigma_{\text{int}}^{\prime 2}$	z'	Chow	
All GRBs	99	-0.98 ± 0.09	49.27 ± 0.32	0.74 ± 0.06	3.26	0.35	-0.72 ± 0.08	47.31 ± 0.36	0.57 ± 0.05	4.80	0.03	-23%
Gold	10	-1.24 ± 0.27	50.37 ± 0.93	0.68 ± 0.21	...	1.00	-1.16 ± 0.27	49.49 ± 1.13	0.55 ± 0.21	...	1.00	-19%
LGRBs	50	-0.91 ± 0.12	49.14 ± 0.42	0.68 ± 0.07	1.18	0.26	-0.72 ± 0.12	47.41 ± 0.53	0.56 ± 0.07	2.15	0.03	-18%
SGRBs	9	-1.00 ± 0.51	48.92 ± 1.71	1.35 ± 0.38	1.78	0.30	-0.72 ± 0.34	46.71 ± 1.54	0.92 ± 0.32	3.31	0.02	-32%
GRB-SNe Ic	14	-0.75 ± 0.15	47.65 ± 0.64	0.57 ± 0.14	4.31	0.001	-0.67 ± 0.18	46.87 ± 0.85	0.58 ± 0.15	2.90	0.03	+2%
GRB-SNe ABC	9	-0.80 ± 0.13	47.91 ± 0.50	0.40 ± 0.13	3.45	0.003	-0.63 ± 0.14	46.80 ± 0.61	0.35 ± 0.13	2.32	0.03	-13%
XRFs	10	-1.06 ± 0.24	49.07 ± 0.96	0.71 ± 0.20	3.47	0.08	-0.67 ± 0.25	46.78 ± 1.12	0.56 ± 0.22	3.14	0.02	-21%
XRRs	31	-1.05 ± 0.17	49.62 ± 0.54	0.77 ± 0.11	1.48	0.75	-0.75 ± 0.14	47.53 ± 0.59	0.56 ± 0.10	2.79	0.24	-27%
Type I GRBs	9	-1.00 ± 0.51	48.92 ± 1.71	1.35 ± 0.38	1.78	0.30	-0.72 ± 0.34	46.71 ± 1.54	0.92 ± 0.32	3.31	0.02	-32%
Type II GRBs	94	-0.99 ± 0.09	49.32 ± 0.31	0.72 ± 0.06	2.91	0.40	-0.70 ± 0.08	47.27 ± 0.34	0.55 ± 0.05	4.31	0.04	-24%

Best-fit Parameters for the Subsamples in 3D with Simple BPL Model												
Class	N	Uncorrected for Evolution					Corrected for Evolution					$\Delta\sigma_{\text{int}}^{\prime 2}$
		a_{opt}	b_{opt}	C_0	σ_{int}^2	z	a'_{opt}	b'_{opt}	C'_0	$\sigma_{\text{int}}^{\prime 2}$	z	
All GRBs	19	-0.84 ± 0.18	0.40 ± 0.13	30.07 ± 6.33	0.52 ± 0.12	...	-0.72 ± 0.19	0.29 ± 0.13	33.98 ± 5.88	0.45 ± 0.12	...	-13%
LGRBs	12	-0.95 ± 0.28	0.34 ± 0.15	33.36 ± 7.11	0.54 ± 0.16	...	-1.00 ± 0.30	0.34 ± 0.17	33.15 ± 7.75	0.51 ± 0.20	...	-2%
XRRs	5	-0.71 ± 0.36	0.39 ± 0.25	19.18 ± 12.33	0.83 ± 0.39	...	-0.37 ± 0.25	0.46 ± 0.22	25.02 ± 10.03	0.33 ± 0.32	...	-60%
Type II	19	-0.76 ± 0.19	0.31 ± 0.13	33.52 ± 6.01	0.44 ± 0.13	...	-0.87 ± 0.19	0.42 ± 0.13	29.41 ± 6.34	0.53 ± 0.13	...	-17%

Note. The first vertical half of the table (left) shows the GRB classes, the normalization, the slope with their respective errors, and the intrinsic scatter σ_{int}^2 for each class for the 2D correlation uncorrected for selection biases. The second vertical half of the table (right) show the same variables, but corrected for selection biases (denoted by $'$). The final column (13) shows the fractional change in σ_{int}^2 among the classes after correcting for redshift evolution and selection biases. In the 2D subtable, columns (6) and (7) (columns (11) and (12)) show the z -score and Chow test p -value, representing two statistical tests comparing subclasses with the Gold fundamental plane without (with) the correction for redshift evolution. Z -scores could not be computed for the 3D case due to the lack of an appreciable Gold sample.

Table 4
The Best-fit Parameters of the 2D and 3D Correlations with the Smoothly BPL Model

Best-fit Parameters for the Subsamples in 2D with the Smoothly BPL Model												
Class	N	Uncorrected for Evolution					Corrected for Evolution					
		a_{opt}	C_0	σ_{int}^2	z	Chow	a'_{opt}	C'_0	σ'^2_{int}	z'	Chow	$\Delta\sigma'^2_{\text{int}}$
All GRBs	45	-0.97 ± 0.10	49.48 ± 0.37	0.74 ± 0.08	0.27	0.49	-0.80 ± 0.11	47.99 ± 0.47	0.62 ± 0.08	1.08	0.68	-16%
Gold	5	-0.57 ± 0.21	48.14 ± 0.86	0.31 ± 0.21	0.00	1.00	-0.65 ± 0.26	47.43 ± 1.24	0.42 ± 0.25	0.00	1.00	+35%
LGRBs	21	-1.04 ± 0.15	49.97 ± 0.58	0.65 ± 0.12	-0.52	0.36	-0.98 ± 0.16	49.01 ± 0.77	0.60 ± 0.14	-0.29	0.38	-8%
SGRBs	4	-1.25 ± 0.72	50.37 ± 2.94	2.23 ± 0.90	0.49	0.72	-0.75 ± 0.46	47.37 ± 2.31	1.34 ± 0.61	1.57	0.59	-40%
GRB-SNe Ic	5	-0.40 ± 0.23	46.75 ± 0.85	0.44 ± 0.22	5.49	0.01	-0.33 ± 0.32	45.82 ± 1.36	0.56 ± 0.33	1.37	0.26	+27%
GRB-SNe ABC	4	-0.69 ± 0.30	47.99 ± 1.22	0.38 ± 0.22	4.91	0.01	-0.66 ± 0.45	47.41 ± 1.91	0.43 ± 0.25	1.23	0.95	+13%
XRFs	4	-0.72 ± 0.29	47.97 ± 1.05	0.77 ± 0.32	3.09	0.12	-0.59 ± 0.32	46.38 ± 1.42	0.81 ± 0.76	4.70	0.09	+5%
XRRs	17	-1.27 ± 0.21	50.27 ± 0.71	0.81 ± 0.15	0.11	0.15	-0.94 ± 0.21	48.38 ± 0.85	0.63 ± 0.14	1.28	0.34	-22%
Type I GRBs	4	-1.25 ± 0.72	50.37 ± 2.94	2.23 ± 0.90	0.49	0.72	-0.75 ± 0.46	47.37 ± 2.31	1.34 ± 0.61	1.57	0.59	-40%
Type II GRBs	44	-0.99 ± 0.11	49.55 ± 0.41	0.75 ± 0.09	0.25	0.45	-0.82 ± 0.11	48.09 ± 0.47	0.63 ± 0.07	1.02	0.67	-16%

Best-fit Parameters for the Subsamples in 3D with Smoothly BPL Model												
Class	N	Uncorrected for Evolution					Corrected for Evolution					
		a_{opt}	b_{opt}	C_0	σ_{int}^2	z	a'_{opt}	b'_{opt}	C'_0	σ'^2_{int}	z	$\Delta\sigma'^2_{\text{int}}$
All GRBs	8	-1.01 ± 0.31	0.31 ± 0.18	34.88 ± 8.30	0.60 ± 0.27	...	-0.71 ± 0.20	0.23 ± 0.11	36.90 ± 5.23	0.34 ± 0.17	...	-38%
Type II	8	-1.01 ± 0.31	0.31 ± 0.18	34.88 ± 8.30	0.60 ± 0.27	...	-0.71 ± 0.20	0.23 ± 0.11	36.90 ± 5.23	0.34 ± 0.17	...	-38%

Note. The first vertical half of the table (left) shows the GRB classes, the normalization, the slope with their respective errors, and the intrinsic scatter σ_{int}^2 for each class for the 2D correlation uncorrected for selection biases. The second vertical half of the table (right) show the same variables, but corrected for selection biases (denoted by '). The final column (13) shows the fractional change in σ_{int}^2 among the classes after correcting for redshift evolution and selection biases. In the 2D subtable, columns (6) and (7) (columns (11) and (12)) show the z -score and Chow test p -value, representing two statistical tests comparing subclasses with the Gold fundamental plane without (with) the correction for redshift evolution. Z -scores could not be computed for the 3D case due to the lack of a sufficiently large Gold sample.

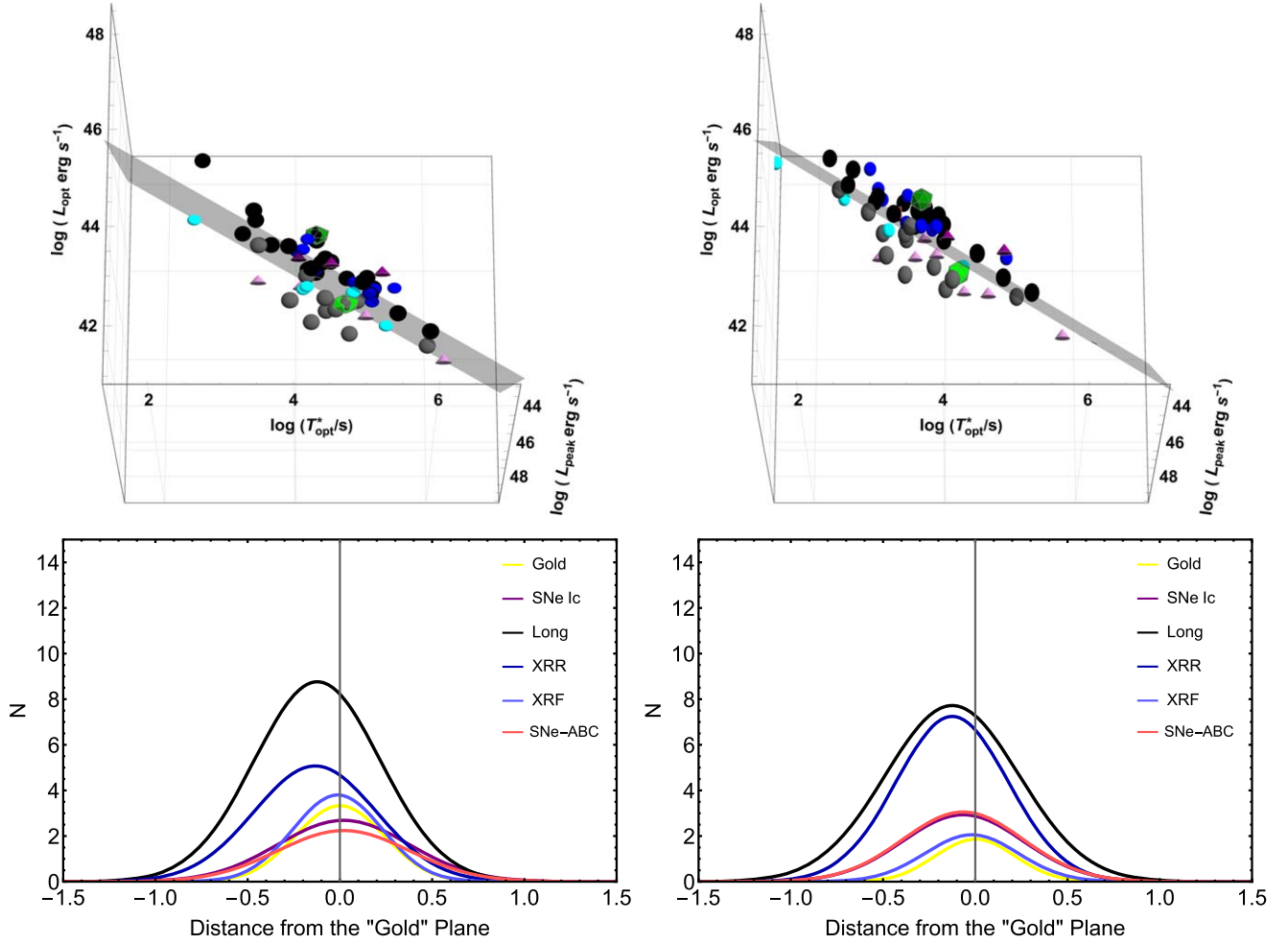


Figure 3. Top panels: 58 GRBs in the $L_{\text{opt}}^{(l)} - T_{\text{opt}}^{(*,l)} - L_{\text{opt}}^{(l)}$ parameter space with the fitted plane parameters in Table 2, including LGRBs (black circles), SGRBs (red cuboids), GRB-SNe Ic (purple cones), XRFs and XRRs (blue spheres), and ULGRBs (green icosahedrons). The left and right panels display the 3D correlation with and without any correction for both redshift evolution and selection biases, respectively. Bottom panels: the distances of the GRB of each class indicated with different colors from the Gold fundamental plane, which is taken as a reference, with and without correction for redshift evolution and selection biases, respectively.

$k_{\text{opt,peak}} = 3.10 \pm 1.60$, and $k_{\text{opt,T}} = -2.09 \pm 0.40$ define the slope of the evolutionary functions. For details about the application of the method, see Dainotti et al. (2013, 2015, 2017b, 2020b).

For the X-ray fundamental plane relation, the correction for evolution is $k_{T_X} = -1.25 \pm 0.28$, for $k_{L_{X,a}} = 2.42 \pm 0.58$ and $k_{L_{\text{peak}}} = 2.24 \pm 0.3$. Thus, the evolutionary parameters for $L_{X,\text{opt}}$ and $T_{X,\text{opt}}$ are within 2σ , while that for $L_{X,\text{opt,peak}}$ is within 1σ .

The derived parameters for each class can be found in Figure 4 and Table 2. The a parameter between the Gold and all samples are compatible with 1σ both for the corrected and uncorrected cases. The a parameter of the uncorrected and corrected correlations in all other classes are compatible with one another within 1σ . The uncorrected b parameter is compatible with all classes with the exception of a few cases. The GRB-SNe Ic are compatible with XRR within 2σ , and GRB-SNe Ic and LGRBs are compatible within 2σ . The corrected b parameter is compatible with all classes with the exception of only LGRBs and XRR, which are compatible within 2σ . The uncorrected and corrected C_0 are all compatible within 1σ except with the uncorrected case in which GRB-SNe Ic and LGRBs are compatible within 2σ .

The last column of Table 2 shows the percentage decrease for all samples compared between the uncorrected and

corrected correlations in 3D. The intrinsic scatter of the corrected variables as compared to those uncorrected for evolution is smaller by at least 4% in the case of the GRB-SNe Ic and up to 36% for the XRR subsample. This illustrates the importance of accounting for selection biases.

4.2. The 2D Optical Relation with the Willingale et al. (2007)

$$\text{Model: } L_{\text{opt}}^{(l)} - T_{\text{opt}}^{(*,l)}$$

From Figure 5 and Table 2, we see that the slope of the 2D correlation uncorrected and corrected for selection biases is compatible within 1σ for all classes with the exception of a few cases. For the uncorrected case XRR and GRB-SNe Ic are compatible within 2σ . For the corrected case the ULGRBs are compatible with the XRFs, SNe Ic, SNe ABC, SGRBs, and the Gold within 2σ . The normalization constants (C_0) are all compatible within 1σ with the exception of a few cases. In the case of the uncorrected C_0 SNe Ic are compatible within 2σ with XRRs, XRFs, LGRBs, and ULGRBs. For the corrected case the ULGRBs are compatible within 2σ with SGRBs, Gold, SNe Ic, SNe ABC, LGRBs, and XRFs. Additionally, SGRBs are compatible within 2σ with XRRs.

We assume that all classes undergo a similar redshift evolution for simplicity because, besides LGRBs, all other

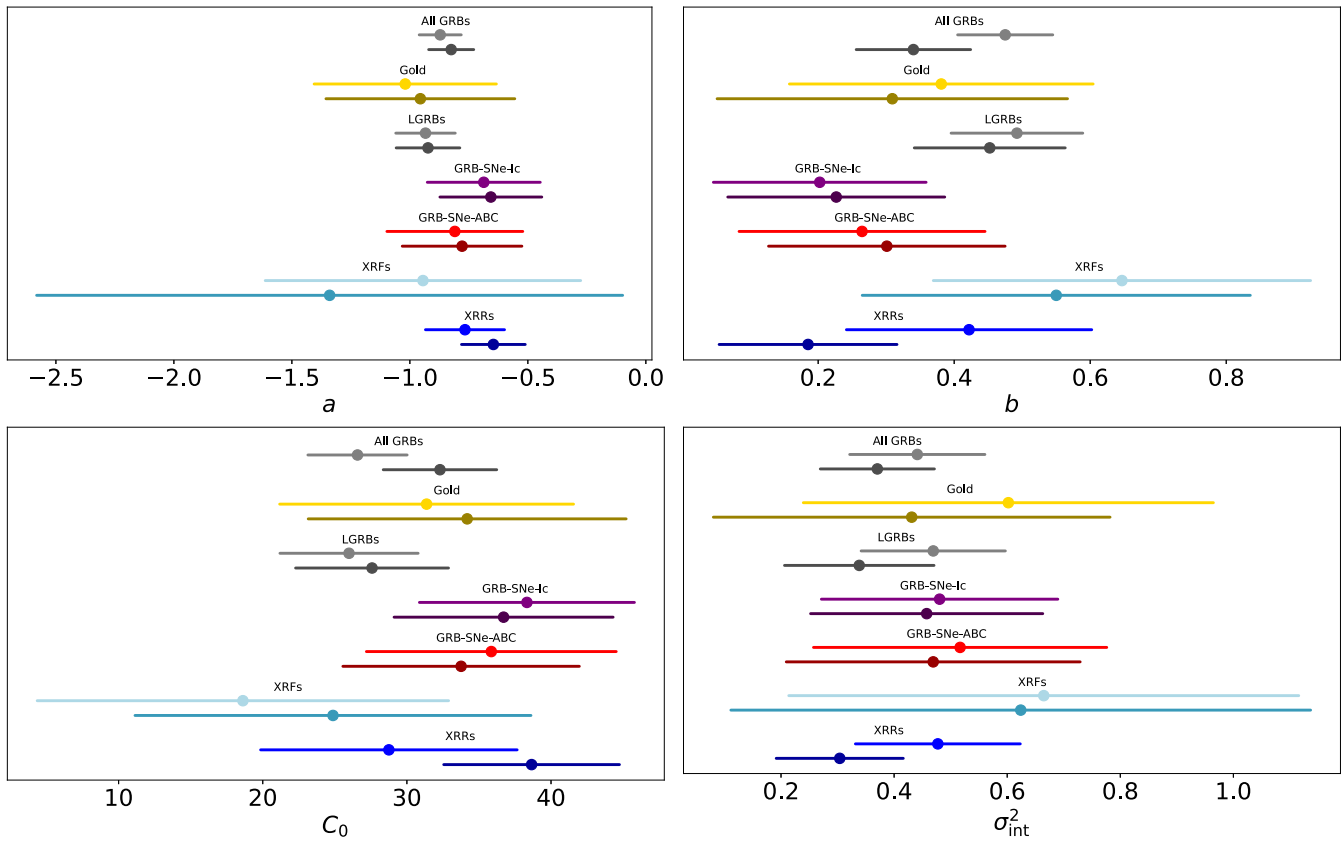


Figure 4. An overview of 3D fundamental plane best-fit parameters, where a , b , and C_0 are color coded according to the GRB class, with darker colors denoting correction. The x-axis displays the 1σ intervals for each parameter. The color coding is as follows: gray for LGRBs, gold for the Gold sample, light blue for XRFs, blue for XRRs, bright green for ULGRBs, purple for SNe Ic, red for SNe ABC, cyan for short and Type I (since both samples are identical), and orange for Type II. The same colors, but darker are for the corrected class. Exact values for each parameter can be found in Table 2.

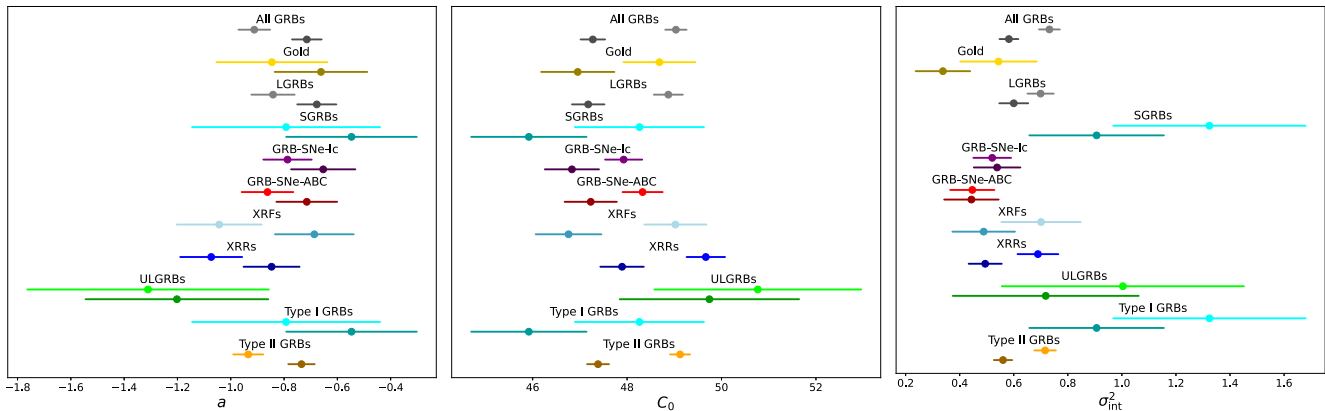


Figure 5. An overview of 2D fundamental plane best-fit parameters, where a and C_0 are color coded according to the GRB class, with darker colors denoting correction. The x-axis displays the 1σ parameter intervals. The color coding is as follows: gray for LGRBs, gold for the Gold sample, light blue for XRFs, blue for XRR, bright green for ULGRBs, purple for SNe Ic, red for SNe ABC, and cyan for both short and Type I (since both samples are identical), and orange for Type II. Exact values for each parameter can be found in Table 2.

classes have too few GRBs to be considered alone to reliably apply the Efron & Petrosian (1992) method. After the correction is applied, all slopes between classes except the ULGRB subsample are compatible within 1σ . The ULGRB sample is compatible with the XRR subsample within 1σ , and 2σ for all other subsamples. The normalization constants are compatible within 1σ except for the ULGRBs, which are compatible with the XRRs within 1σ and with all other classes within 2σ .

This highlights an important finding: the GRB classes are not distinguishable in terms of the parameters of the 2D optical correlation both with and without correction for selection biases and redshift evolution. The fact that the classes are indistinguishable is checked with the z -score. This trend is different in the 2D and 3D X-ray correlations, where these classes are distinguishable (Dainotti et al. 2010, 2017a, 2017b, 2020b).

4.3. The 2D and 3D Correlations with the BPL Functions

Here, we repeat the fitting of the selected 179 GRBs with the BPL with the requirement that the angle of the plateau should be less than 41° , corresponding to $|\alpha_1| < 0.8$, and found that 99 GRBs can be appropriately fitted with a simple BPL (Equation (5)), while 45 can be fitted with a smoothly BPL (Equation (6)). The results of fitting the simple and smoothly BPL models in 2D and in 3D are shown in Tables 3 and 4.

Checking the agreement of the parameters for the simple BPL correlation in 2D, we find the slope of the uncorrected correlation a_{opt} of the Gold sample agrees with all other classes within 1σ except for the GRB-SNe Ic and GRB-SNe ABC, which agree within 2σ . For the corrected correlation, the slope of the Gold sample is compatible with SGRBs, XRFs, and XRRs within 1σ —all other classes (LGRBs, GRB-SNe Ic, GRB-SNe ABC) are compatible within 2σ . The normalization constant C_0 of the uncorrected correlation for the Gold sample is compatible with all classes within 1σ except for the GRB-SNe Ic, and GRB-SNe ABC for which it is compatible within 2σ . For the corrected correlation, the C_0 of the Gold sample is compatible with all classes within 2σ .

For the 3D simple BPL correlation, we instead compare the classes to the total sample, as there are too few data points to define a Gold sample. The slope a_{opt} and b_{opt} parameters of both the corrected and uncorrected correlations are compatible with all classes within 1σ . The C_0 parameter is similarly compatible with all classes in all cases except for the corrected LGRBs, which are compatible with the corrected total sample within 2σ .

For the smoothly BPL in 2D, the slope and normalization parameter of the uncorrected correlation in the Gold sample are compatible with all classes within 1σ except the LGRBs and XRRs, which are compatible within 2σ . The slope and C_0 of the corrected Gold sample are compatible with all other classes within 1σ .

The 3D correlation sample only contains eight GRBs, which are all classified as Type II GRBs, so we do not conduct the same analysis.

4.4. The Distance from the Gold Fundamental Plane

Following Dainotti et al. (2021a), we test if the fundamental plane can be a discriminant between classes within the W07 samples. In each 2D and 3D sample, we compute the distance of any GRB class from the plane identified by the Gold sample for both corrected and uncorrected GRBs via calculating a z -score, which is defined as

$$z = \frac{\mu - \mu_{\text{Gold}}}{\sqrt{(\sigma/\sqrt{N})^2 + (\sigma_{\text{Gold}}/\sqrt{N_{\text{Gold}}})^2}}, \quad (9)$$

where μ denotes the mean, σ the standard deviation, and N the number of points in a given sample (see the bottom panels of Figure 3). We find that in the uncorrected 2D W07 correlation, there is a significant indication ($|z^{(i)}| > 3$) of differences between classes and the Gold plane with the GRB-SNe Ic and GRB-SNe ABC, at $z = 5.23$ and 4.34 , respectively. This result is expected because indeed in X-rays, the 2D correlation (Dainotti et al. 2017b) for the GRB-SNe ABC subsample of seven GRBs has a slope of -1.9 and a slope of -1.5 with 19 GRBs associated with all GRB-SNe Ic types. The sample size in the current investigation for GRB-SNe Ic is 26 (27%

increase) and 19 (92% increase) for the GRB-SNe ABC. This result then shows that with a much larger sample that the GRB-SNe Ic may behave differently from the regular LGRBs in terms of the 2D correlation and the energy reservoir may not be constant any longer for these classes. However, this result becomes insignificant even at the 2σ level, so it may possible that this is due to redshift evolution.

Interestingly, after correcting the sample for redshift evolution and selection biases, the magnitude of the z -scores are reduced, but still indicate some difference ($z \approx 2-3$) between the Gold sample and the Type I SGRB and XRF subsamples. Exact z -values can be found in Table 2. The uncorrected 2D z -scores range from -2.39 to 5.23 for W07, from 1.18 to 4.31 for the simple BPL, and from -0.52 to 5.49 for the smoothly BPL. For the corrected 2D correlation, the z -scores range from -1.75 to 2.17 for W07, from 2.15 to 4.80 for the simple BPL, and from -0.29 to 4.70 for the smoothly BPL.

Here, we notice that the range of variations of the z -scores for the 2D uncorrected sample is largest for W07, while the variation of the z -scores for the corrected 2D sample is largest for the smoothly BPL. The simple BPL carries the minimum change of variation in both the corrected and uncorrected cases.

The uncorrected 3D z -scores range from -1.04 to 0.19 for W07, while the corrected 3D z -scores range from -0.94 to 0.10 . We find no significant indication of differences between classes from the Gold plane (see Figure 3).

This analysis would benefit from an increased sample, as z -scores are being penalized for large σ and small sample sizes. With a larger sample, we may be able to use the 3D optical fundamental plane as a class discriminator, similarly to the X-ray fundamental plane.

We also test if this total sample of 179 GRBs still holds the same features in terms of each class (top panels of Figure 6), the presence of the Gold sample (second row), groupings of plateau angles (third row of panels). The left panels of these three rows show the correlations without correction for selection biases and redshift evolution, while the right panels show the correlations after correction. We also investigate if there is clustering in terms of type I and II GRBs in the bottom left panel and in the case of GRB-SNe Ic and GRB-SNe-ABC (bottom right panel). Similar to Dainotti et al. (2021a), there is no particular clustering of GRBs around any given class, plateau angle, nor within the Gold sample. This occurs within the total sample both with and without the correction for redshift evolution and selection biases. These GRB features are less distinguishable compared to those in X-rays (Dainotti et al. 2021a).

4.5. The Anderson–Darling, Anderson, and Chow Tests

We also test if the functional relationship is valid with the Anderson–Darling test by checking the null hypothesis that $L_{a,\text{opt}}$ is drawn by the same population as the $L_{\text{opt,theor}}$ distribution as determined by the 2D and 3D correlations of each total sample. In 3D, if we consider the W07 function and the BPL functions for both the corrected and uncorrected correlations, we find that for all functions, the null hypothesis is heavily favored with $p \geq 0.25$ for both the uncorrected and corrected correlations.

In 2D correlations, we find that the uncorrected correlation in the simple BPL fitting again favors the null hypothesis at $p = 0.25$. In contrast, the corrected correlation accepts the null

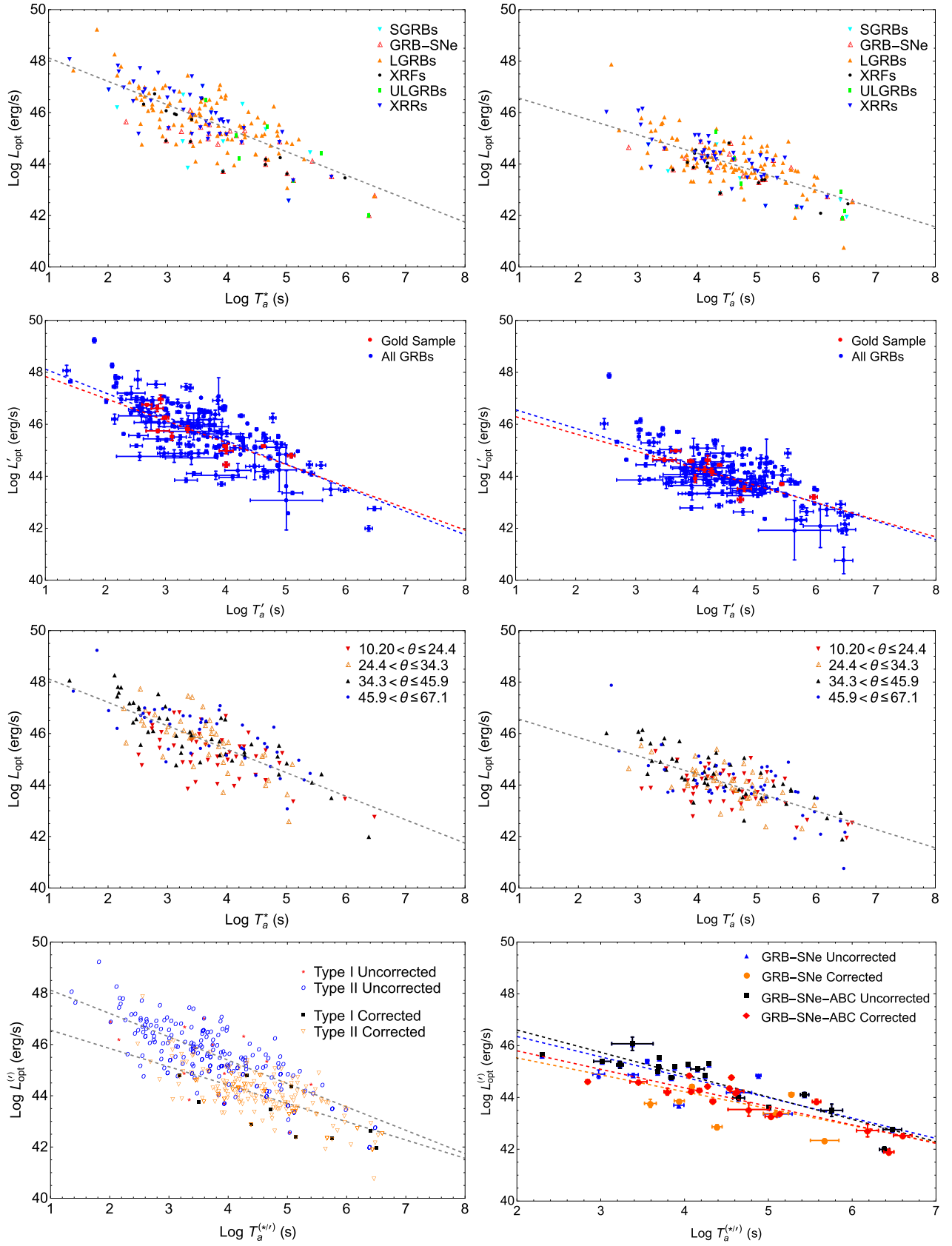


Figure 6. The three top left panels show the observed $L_{\text{opt}}^{(*)} - T_a^{(*)}$ correlations uncorrected for biases and evolution with all classes (first row), the total and Gold samples (second row), and plateau angles (third row), respectively. Panels on the left for the first three rows show the correlation without any correction, on the right with correction. The bottom left panel shows Type I and Type II GRBs. The bottom right shows the GRB-SNe Ic and GRB-SNe ABC classes before and after correction.

hypothesis at 12%. The smoothly BPL fitting favors the null hypothesis at 25% for both the corrected and uncorrected correlations. When we apply the test W07 function, we obtain that the null hypothesis is favored at the 9% level for the uncorrected sample and the corrected one.

We also applied the Anderson test for normality (or Gaussianity)²⁸ of best-fit residuals ($L_{\text{opt,observed}} - L_{\text{opt,theor}}$). For both the corrected and uncorrected 3D correlation in all models, and regardless of the fitting procedure, the null hypothesis (that the distribution is drawn from a Gaussian) is accepted at $p > 15\%$, with the exception of the corrected W07 sample, which is still accepted at a p -value of 0.12. For the 2D correlations, both the smoothly and simple BPLs, as well as the corrected W07 correlation, are accepted at the $p > 15\%$ level. The uncorrected W07 fitting is accepted at the $p > 10\%$ level. Thus, we can safely state that in all cases, the 2D and 3D correlations do fulfill both the test of Gaussianity and the Anderson–Darling test for verifying the true nature of the correlation.

Although we have presented the values of the z -scores and have shown the compatibility among all classes in the 2D relations, it may be valuable to consider additional statistical tests so that we can draw more reliable conclusions. We stress that parameter confidence interval calculations are based on asymptotic theory. For discussion of multiple regression with small samples, see the discussion and references in Kelley & Maxwell (2003). We assume the regression models in Equation (3), (5), and (6) are correct.

We apply the Chow test (Chow 1960) to verify whether the true coefficients in two linear regressions between different subsamples and the Gold sample are equal. In parallel with the z -score test, we take the Gold sample as a reference. We compute the Chow test p -values for the several classes against the Gold sample both for the cases of the W07 and both BPL models in 2D, and for both the cases with and without correction for evolution and selection biases. Due to the lack of an appreciable Gold sample for the simple and smoothly BPLs, the Chow test was not computed in the 3D case.

We first discuss the 2D relation without the correction for redshift evolution and sample bias. From the Chow test results for the W07 sample with no evolution, we can assess that the Gold and full sample have similar coefficients with the highest probability of 87%; the Gold sample also has similar coefficients to the SGRBs/Type I at 84% and the Type II GRBs at 81%. The classes of GRBs associated with GRB-SNe Ic, GRB-SNe ABC, and XRFs have coefficients that are the least similar to the Gold sample at 5%, 16%, and 22%, respectively. The GRB-SNe Ic and GRB-SNe ABC show a smaller percentage of agreement with the Gold sample, and this is aligned with the idea explained in the 1 that the GRB-SNe may not be following the same trend as the regular GRBs for which the SNe have not been seen. The rest of the classes yield similar parameters with $p \geq 60\%$ (see Table 2). Interestingly and unexpectedly, the SGRBs have the highest probability of the parameters being similar after the total sample. When we consider the simple BPL sample for the case without correction for evolution, the results are, as expected, comparable with the one with W07, though the most similar class to the Gold sample is the XRRs, with a probability of 75%. The Chow p -value for all other classes is $< 60\%$, the smallest being the

GRB-SNe Ic and GRB-SNe ABC subsamples with p -values of 0.1% and 0.3%, as seen in W07. The low value of probability for these classes further strengthens the idea that the GRB-SNe population may follow a different trend compared to the regular LGRBs.

Additionally, in considering the smoothly BPL sample, we see that the p -values show the same trend as the W07 and simple BPL samples. In this case the Chow p -value for the short GRB sample is the largest (72%) and it is followed by the Type II GRBs (45%), as in W07. Nevertheless, in all cases, the GRB-SNe Ic, GRB-SNe ABC, and XRF subsamples represent the lowest p -values of all tests within the context of samples uncorrected for evolution.

After correcting for evolution in all three samples, p -values tend to have less spread among each class. For the W07 fitting, the full sample still has the highest probability at 92%, and it is still followed by Type II at 86% and SGRBs/Type I at 67%. The XRF now has the lowest similarity, with a probability of 18%, while the other classes range from 42% to 63% probability. Considering the simple BPL fitting, the spread of values lessened considerably—the XRR has the greatest similarity to the Gold sample with 24% probability, while the XRF and SGRB/Type I have the lowest similarity at 2%. The other classes range from 3% to 4% probability. For the smoothly BPL, the GRB-SNe ABC now have the highest probability (95%), while the XRF has the lowest probability (9%), as in W07. The Type II are the second highest at 67% probability, and the other classes range from 26% to 59% probability (see Tables 2, 3, and 4 for exact values.)

It is interesting to note that although the p -values vary from the BPL and the W07 functions, the conclusion of the analysis remains the same within the uncorrected fittings and corrected fittings, thus supporting the reliability of these conclusions, which are independent from the functional forms used for fitting the LCs.

5. Comparison between Optical and X-Rays

5.1. Discussion of the Current Status in the Literature

GRB collimation has been inferred with the observations of achromatic steepening in GRB LCs, such steepenings are called jet breaks. Pinpointing a jet break from afterglow LCs enables us to measure the jet opening angle and consequently the GRBs' energy. Investigating which GRBs are chromatic and achromatic is crucial for tackling this issue. The topic of the achromaticity versus chromaticity of the LCs in X-rays and optical has been extensively studied in the literature (Panaitescu et al. 2006; Huang et al. 2007; Liang et al. 2007; Molinari et al. 2007). To be more specific in Panaitescu et al. (2006) several GRBs such as 050319, 050401, 050607, 050713A, 050802, and 050922C exhibit a steepening at 1–4 hr in X-rays after the burst, which, surprisingly, is not accompanied by a break in the optical emission. The reason for this behavior is still a puzzling issue. Out of the several GRBs presented in Panaitescu et al. (2006) we have four GRBs that are also common to our sample: 050401, 050319, 050802, and 050922C. Most likely, the behavior of not being accompanied by the spectral break does not originate from the outflow collimation. If the optical and X-ray observations stem from the same synchrotron forward-shock model, we identify the temporal breaks with the passage of the synchrotron cooling break through the X-ray band. That evolution of the synchrotron cooling break depends

²⁸ The Anderson–Darling and Anderson tests have been performed with the `scipy` Python package.

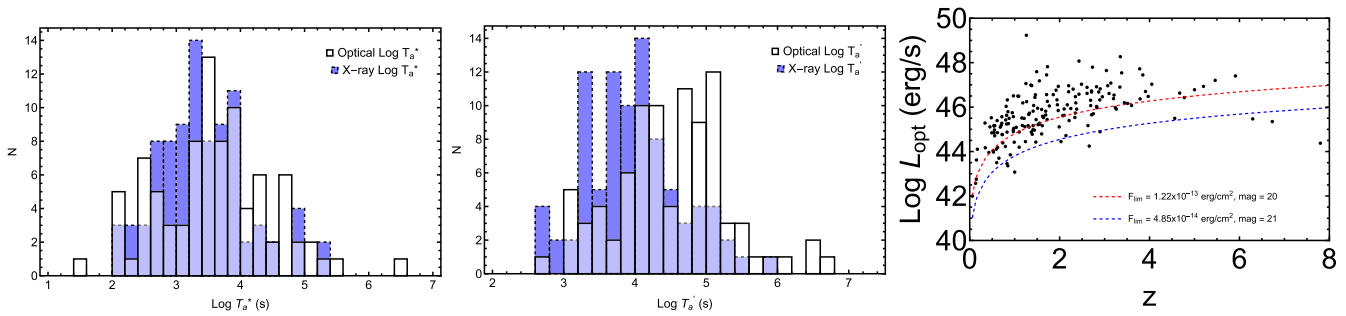


Figure 7. Left panel: the differential distribution of $T_{X,a}^*$ (white solid line) and $T_{opt,a}^*$ (blue dashed line). Middle panel: the same as the left panel, but corrected for evolution. Right panel: the observed luminosity vs. redshift with limiting luminosity curves given by the observability with Tomo-e Gozen.

on the equivalent kinetic energy, circumburst density, micro-physical parameters, and the electron population’s spectral index. It is worth noting that a temporal break in the optical observations without observing a temporal break in the X-rays could also be explained by the passage of the spectral break in optical bands. Liang et al. (2007) analyzed the origin of the shallow X-ray phase in a sample of 53 long bursts detected by Swift. Among the 13 bursts with well-sampled optical LCs, six had an optical break, t_b , consistent with being achromatic. However, the remaining cases either did not show an optical break or had a break at an epoch different from t_b . This observational result poses challenges for the synchrotron forward-shock scenario with energy injection, opening up to the possibility that the optical and X-ray emission may not be emitted by the same mechanism, at least for some bursts. There are four significant outliers in the sample, GRBs 060413, 060522, 060607A, and 070110. The last two bursts are also present in our sample. A very steep decay immediately follows the shallow decay phase exhibited in these X-ray light curves after t_b , which is inconsistent with any external shock model. The optical and X-ray observations show that these bursts evolve independently, indicating these X-ray plateaus may have an internal origin (Troja et al. 2007; De Pasquale et al. 2016).

However, a one-to-one comparison among the GRB light curves in X-rays and optical is needed to determine more realistically whether or not we have an achromatic or chromatic plateau.

In Liang et al. (2007) at least some X-ray breaks are chromatic. In the current paper we check consistency of the chromaticity versus achromaticity scenario for 89 GRBs that have both X-ray and optical light curves. As a result, we have 10 cases of achromatic emission when we do not correct for selection biases and redshift evolution and 13 cases when we apply these corrections. The achromatic cases, which are a fraction of 11.2% in case of no evolution and 14.6% in case of evolution may reflect that these are associated with an external origin (e.g., refreshed shocks). However, the remaining cases cannot be explained within this scenario.

Invoking different emission regions (e.g., Zhang & Meszaros 2002) may solve the problem, although more detailed modeling is needed. Crossing a cooling break would also result in a temporal break, but it would also be accompanied by a spectral index variation by ~ 0.5 . Liang et al. (2007) found that the changes in the X-ray spectral indices across the breaks of GRB 050318, 050319, 050802, and 050401 are between 0.01 and 0.12, and therefore much smaller than 0.5. Thus, the suggestion of a cooling spectral break is ruled out. Genet et al. (2007) accounted for these chromatic breaks as being due to a

long-lived reverse shock in which only a small fraction of the electrons are accelerated. The main issue for such an interpretation is how to “hide” the emission from the forward shock, which carries most of the energy.

Molinari et al. (2007) analyzed the cases of GRB 060418 and GRB 060607A and concluded regarding GRB 060418 that due to the difference between the spectral indices in X-rays, β_X , and near-infrared, β_{NIR} , a different origin for those wavelengths may occur. For the case of GRB 060607A a definite conclusion cannot be reached due to the presence of flares. Wang et al. (2015, 2018) used a large sample of GRBs that have an optical break consistent with being achromatic in the X-ray band. Their sample includes 99 GRBs from 1997 February to 2015 March that have optical and X-ray LCs for Swift GRBs. These X-ray LCs are consistent with the jet break interpretation. Out of these 99 GRBs, 55 GRBs have temporal and spectral behaviors both before and after the break, consistent with the theoretical predictions of the jet break models, respectively. These include 53 long/soft (Type II) and 2 short/hard (Type I) GRBs.

5.2. The Analysis in This Paper

Because the above discussions are based on a one-to-one comparison, we follow two approaches in this work: the first one is to show the distribution of the sample to study the population as a whole, shown in the left and middle panels of Figure 7, and the second approach is to perform a one-to-one analysis in which we show the plot of T_X versus T_{opt} to highlight the coincidence of the breaks in Figure 8.

Following Dainotti et al. (2021a), we test if the rest-frame end times ($T_a^{(*//)}$) of the plateau are achromatic in X-rays and optical.

The left panels of Figure 8 show the cases without evolution, while the right panels show the cases with evolution. We have shown the uncertainties as ellipses because they are not independent. We also show two examples of the LC comparison between X-ray and optical in that figure. We mark T_a as vertical lines, denoted in red for X-ray and blue for the optical. Specifically, we show two cases in which the plateau seems to show chromaticity (the middle panels of Figure 8) and two cases of achromaticity (bottom panels of Figure 8) within 1σ . We then perform the Kolmogorov–Smirnov test for the uncorrected $T_{X,a}^*$ and $T_{opt,a}^*$ and the corrected $T_{X,a}^{(*//)}$ and $T_{opt,a}^{(*//)}$ distributions. We find that, for times not corrected for evolution or selection biases, the distance among these distributions, D , is $D = 0.20$ with a probability that they are drawn by the same parent population $P = 0.05$. However, when we correct for selection biases and redshift evolution the null hypothesis is

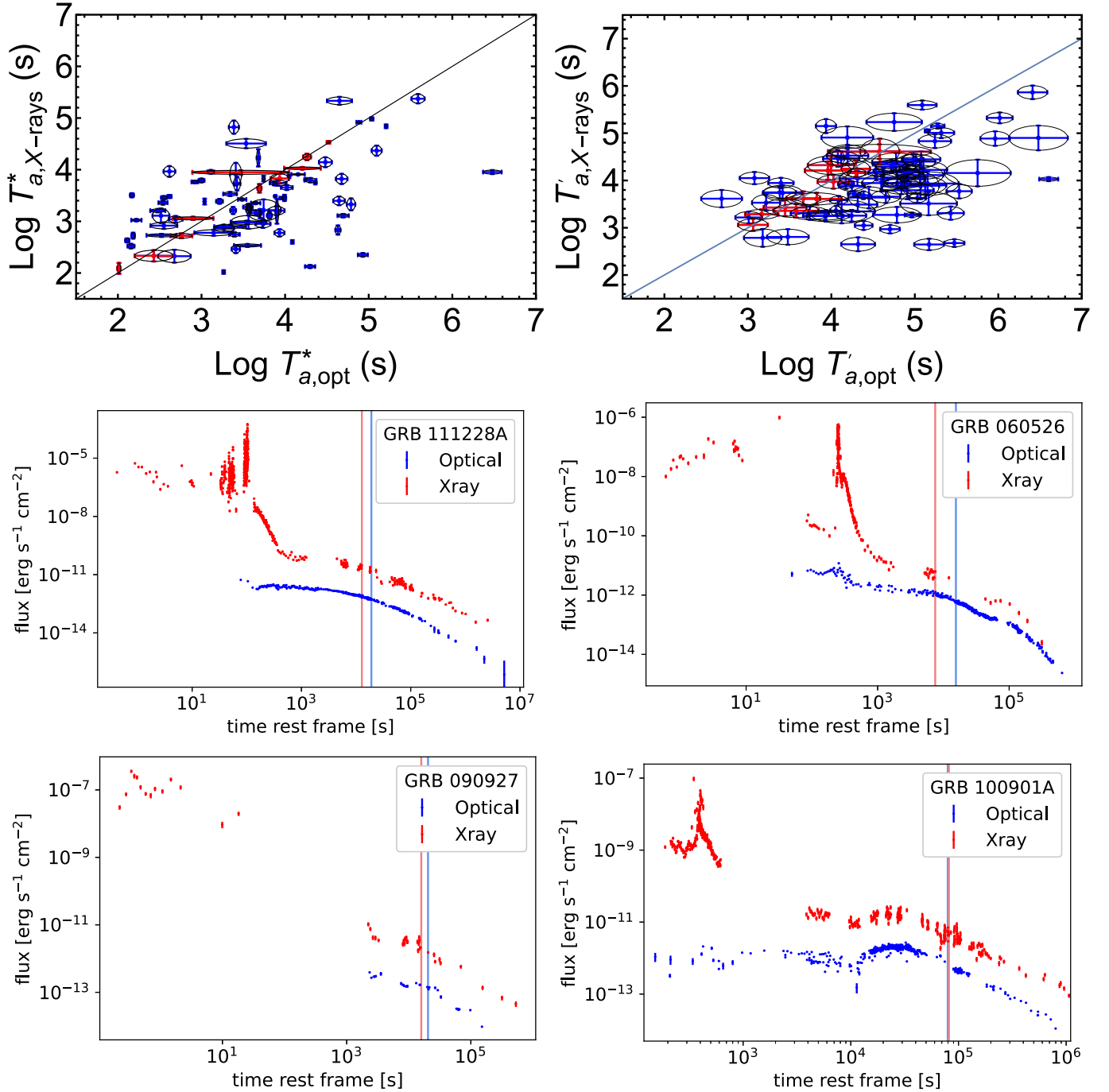


Figure 8. Top left panel: plot of T_{aX}^* vs. $T_{a,opt}^*$ for uncorrected data. Top right panel: the same as the top left panel, but for corrected data. Middle panels: example of GRBs in which the plateau is chromatic in more than 1σ between the X-ray and optical LCs. Bottom panels: examples of GRBs in which the plateau is achromatic between the X-ray and optical LCs within 1σ . T_a^* from the W07 fitting appears as a vertical line, denoted in bright red for X-ray and bright blue for the optical in both the middle and bottom panels.

clearly rejected with $D = 0.36$ and $P = 1.66 \times 10^{-5}$, showing that T_a' is chromatic across X-ray and optical bands, with the observed X-ray breaks happening earlier than those in the optical. This points toward the hypothesis that the end of the plateaus may be associated with an external origin, indicating that the continuous energy injection has finished (e.g., see Lü & Zhang 2014).

We compute the 2D correlation in X-rays for 89 GRBs in common between the X-ray and optical sample; see the left panel of Figure 9, obtaining $a_X = -1.17 \pm 0.10$ and

$a_{opt} = -0.93 \pm 0.09$. After correcting for observational biases and redshift evolution, we find $a'_X = -0.94 \pm 0.13$ and $a'_{opt} = -0.67 \pm 0.08$; see the right panel of Figure 9. In both the corrected and uncorrected cases, the slope agrees within 2σ .

It is clear from this analysis that we need to increase the number of observations to be able to tell whether the uncorrected end-time distributions are chromatic across X-ray and optical wavelengths. Thus, we will soon start an observational campaign for optical GRB follow-up with Tomo-e Gozen, a wide-field CMOS camera mounted on the

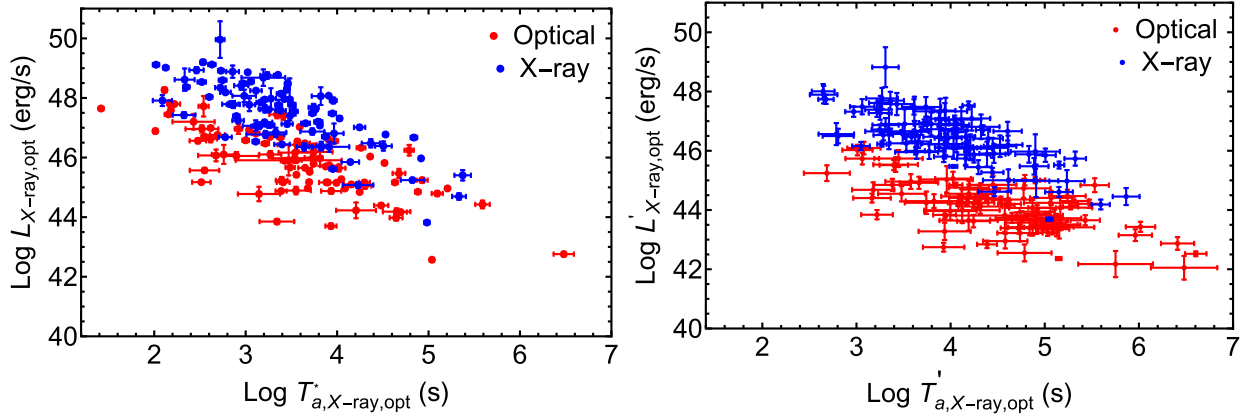


Figure 9. Left panel: plot of $L_{X,a}$ and $L_{opt,a}$ vs. $T_{X,a}^*$ and $T_{opt,a}^*$ in X-ray (blue) and optical (red). Right panel: same as the left panel, but corrected for evolution.

1.05-m KISO Schmidt telescope located in Nagano, Japan (Sako et al. 2018). We show the limiting luminosities of Tomoe Gozen at each redshift, assuming we can detect at 20 mag with an exposure time of 100 s, corresponding to $F_{lim} = 1.22 \times 10^{-13} \text{ erg cm}^{-2} \text{ s}^{-1}$ (red dashed line in Figure 7) and with a 21 mag afterglow and an exposure time of 1000 s, corresponding to $F_{lim} = 4.85 \times 10^{-14} \text{ erg cm}^{-2} \text{ s}^{-1}$ (blue dashed line in Figure 7). If we consider our sample with redshift with an exposure of 1000 s or more, we can observe the majority of bursts with plateau emission. We have also initiated an international collaboration with DDOTI (Watson et al. 2016) where we have similar limiting luminosities as the ones from the KISO and the Telescope in Krakow CDK 500 within the Skynet network for joint observations. The limiting magnitude of the telescope in Krakow is 18 mag (corresponding to $F_{lim} = 1.31 \times 10^{-12}$ in the V band) when the condition of observations are favorable. Based on the current sample of 179 GRBs, we estimate that with the CDK 500 we will still be able to catch a good fraction of the high-luminosity plateaus (36%). The great advantage of this synergy is that the three telescopes are located in three different parts of the world (Europe, Mexico, and Japan) thus allowing a good coverage of the GRB afterglows if they are observable in three locations.

6. Discussion and Conclusions

We have gathered the largest compilation of optical plateaus to date (179 GRBs, 76% larger than the previous sample presented in Dainotti et al. 2020a) and show that the $L_{opt}^{(i)} - T_{opt}^{(*'i)}$ correlation holds, and is compatible with the previous X-ray sample within 1σ both before and after correcting for redshift evolution and selection biases. We also discover the existence of a 3D optical correlation, an extension of the 2D correlation by adding the peak prompt luminosity, $L_{peak,opt}$.

The optical correlation in 3D fitted with W07 model is

$$\log L_{opt} = (-0.87 \pm 0.09) \log T_{opt}^* + (0.48 \pm 0.07) \log L_{peak} + (26.57 \pm 3.44) \quad (10)$$

with $\sigma_{int}^2 = 0.44 \pm 0.12$. For the case of the simple BPL, $a = -0.84 \pm 0.18$, $b = 0.40 \pm 0.13$, $C_0 = 30.07 \pm 6.33$, and $\sigma = 0.52 \pm 0.12$. For the case of the smoothly BPL, $a = -0.97 \pm 0.25$, $b = 0.30 \pm 0.16$, $C_0 = 35.45 \pm 7.68$, $\sigma = 0.55 \pm 0.25$. The 3D correlation fitted with W07 after correcting for

selection biases and redshift evolution is

$$\log L'_{opt} = (-0.82 \pm 0.10) \log T'_{opt} + (0.34 \pm 0.08) \log L'_{peak} + (32.30 \pm 3.94) \quad (11)$$

with $\sigma_{int}^2 = 0.37 \pm 0.10$. Similarly, we find that the parameters for the corrected simple BPL sample are $a' = -0.72 \pm 0.19$, $b' = 0.29 \pm 0.13$, $C_0 = 33.98 \pm 5.88$, and $\sigma' = 0.45 \pm 0.12$. For the corrected smoothly BPL sample, we find that $a = -0.71 \pm 0.20$, $b = 0.23 \pm 0.11$, $C_0 = 36.90 \pm 5.23$, and $\sigma = 0.34 \pm 0.17$. The 3D fundamental plane fitted with W07 for the whole sample corrected for evolution has a σ_{int}^2 16% smaller than the 3D correlation for the uncorrected sample. When we consider the simple and smoothly BPL models, the reduction of scatter is 13% and 38% smaller, respectively. For the 3D Gold sample, fitted with W07, the corrected $\sigma_{int}^2 = 0.43$, which is 28% smaller than the uncorrected $\sigma_{int}^2 = 0.60$.

Regarding the 2D fitting, for the corrected Gold sample, $\sigma_{int}^2 = 0.34$ is 37% smaller than the Gold sample without this correction ($\sigma_{int}^2 = 0.54$) for W07; for the case of the simple and smoothly BPL models, σ_{int}^2 is 19% and 16% smaller, respectively. Similarly to what has been discussed in Dainotti et al. (2020a), the 2D correlation for the uncorrected and corrected Gold samples has a σ_{int}^2 23% and 36% smaller than the corresponding σ_{int}^2 for the full sample, respectively. For the simple BPL, the uncorrected Gold sample has a σ_{int}^2 that is 8% smaller than the full sample, while the corrected Gold sample has a σ_{int}^2 that is 4% smaller than the corrected full sample. For the smoothly BPL, the uncorrected Gold sample has a σ_{int}^2 that is 58% smaller than the full sample, while the corrected Gold sample has a σ_{int}^2 that is 32% smaller than the full sample.

Comparing between the 2D and 3D optical correlations for the W07 sample, the total sample uncorrected for biases for 3D has a σ_{int}^2 40% smaller than the corresponding 2D correlation. Similarly, the 3D correlation for the total sample corrected for selection biases has a σ_{int}^2 36% smaller than the corresponding corrected 2D correlation.

Thus, with our new definition, the Gold sample still reduces the scatter of 2D correlation both before and after correction for selection biases and redshift evolution. Given that the slope of each 2D correlation is nearly -1 , it is implied that the plateau has a fixed energy reservoir independent of a given class. This can be explained within the magnetar scenario. Additionally,

we find that the $L_{\text{opt}}^{(l)} - T_{\text{opt}}^{(*\prime\prime)} - L_{\text{peak}}^{(l)}$ correlation holds regardless of GRB class and plateau angle (Table 2, 3, and 4).

Furthermore, we find that T_a^* is achromatic between X-ray and optical observations for a subsample of GRBs observed at both wavelengths (Figure 7) if we do not consider selection biases for 10 cases and 13 cases when we consider evolution. An underlying chromatic behavior between the X-rays and optical (T_a^l) is shown regardless of correction for selection biases and redshift evolution. This investigation casts a new light in the long-standing debate whether or not the plateau is achromatic in nature. The chromaticity of the plateau between X-rays and optical is aligned with the result of GRB 090510 in which the plateau is chromatic between the Fermi-LAT in high-energy γ -rays and the X-ray observations (Dainotti et al. 2021b).

This work made use of data supplied by the UK Swift Science Data Centre at the University of Leicester. We are particularly grateful to Y. Niino for his precious discussion on the observability and limiting luminosity of the Tomo-e Gozen. We are particularly grateful to T. Sakamoto for the suggestions on the structure of the paper and to T. Moriya for the discussion on the spectral index and on the GRB-SNe classes distinction. We thank G. Sarracino for his help in modifying our host extinction code in Python and R. Fatima for performing some of the fitting; J. Oska, G. Krz el, Z. Kania, C. Wala, S. Gupta, N. Osborne and E. Johnson for data gathering; A. Rabda, N. Osborne, and D. Zhou for the fitting of some GRB LCs; and B. Simone for help with conversions. D.A.K. acknowledges support from Spanish National Research Project RTI2018-098104-J-I00 (GRBPhot). S.Y. and D.L. acknowledge the support by the United States Department of Energy in funding the Science Undergraduate Laboratory Internship (SULI) program. We thank E. Cuellar for his work in managing the SULI summer program. S.Y. gratefully acknowledges the support of the Vagelos Challenge Award at the University of Pennsylvania. R.L.B. acknowledges support from the DGAPA/UNAM IG100820 and the DGAPA/UNAM post-doctoral fellowship. N.F. acknowledges support from the DGAPA/UNAM IN106521. Some of the data used in this paper were acquired with the RATIR instrument, funded by the University of California and NASA Goddard Space Flight Center, and the 1.5-meter Harold L. Johnson telescope at the Observatorio Astron mico Nacional on the Sierra de San Pedro M rtir, operated and maintained by the Observatorio Astron mico Nacional and the Instituto de Astronom a of the Universidad Nacional Aut noma de M xico. Operations are partially funded by the Universidad Nacional Aut noma de M xico (DGAPA/PAPIIT IG100414, IT102715, AG100317, IN109418, IG100820, IN106521, and IN105921). We acknowledge the contribution of Leonid Georgiev and Neil Gehrels to the development of RATIR. M.F., L.Z., and A.Z. are grateful for the support from the Scientific Caribbean Foundation. E.S. thanks the Latino Education Advancement Foundation for their support.

Software: dustmaps (Green 2018), astroquery (Ginsburg et al. 2019), scipy (Virtanen et al. 2020)

ORCID iDs

M. G. Dainotti <https://orcid.org/0000-0003-4442-8546>
 S. Young <https://orcid.org/0000-0002-2488-1899>
 L. Li <https://orcid.org/0000-0002-1343-3089>

D. Levine <https://orcid.org/0000-0003-3411-6370>
 K. K. Kalinowski <https://orcid.org/0000-0001-9825-7418>
 D. A. Kann <https://orcid.org/0000-0003-2902-3583>
 S. R. Oates <https://orcid.org/0000-0001-9309-7873>
 N. Fraija <https://orcid.org/0000-0002-0173-6453>
 R. L. Becerra <https://orcid.org/0000-0002-0216-3415>
 A. M. Watson <https://orcid.org/0000-0002-2008-6927>
 N. R. Butler <https://orcid.org/0000-0002-9110-6673>
 J. J. Gonz lez <https://orcid.org/0000-0002-3724-1583>
 J. X. Prochaska <https://orcid.org/0000-0002-7738-6875>
 E. Ramirez-Ruiz <https://orcid.org/0000-0003-2558-3102>
 M. G. Richer <https://orcid.org/0000-0003-4757-1153>
 S. Zola <https://orcid.org/0000-0003-3609-382X>

References

- Abbott, B. P., Abbott, R., Abbott, T. D., et al. 2017a, *ApJL*, 848, L13
 Abbott, B. P., Abbott, R., Abbott, T. D., et al. 2017b, *ApJL*, 848, L12
 Ahumada, T., Singer, L. P., Anand, S., et al. 2021, *NatAs*, 5, 917
 Avni, Y. 1976, *ApJ*, 210, 642
 Beskin, G., Karpov, S., Bondar, S., et al. 2010, *ApJL*, 719, L10
 Bessell, M. S., Castelli, F., & Plez, B. 1998, *A&A*, 333, 231
 Blake, C. H., Bloom, J. S., Starr, D. L., et al. 2005, *Natur*, 435, 181
 Bloom, J. S., Frail, D. A., & Sari, R. 2001, *AJ*, 121, 2879
 Cannizzo, J. K., & Gehrels, N. 2009, *ApJ*, 700, 1047
 Cannizzo, J. K., Troja, E., & Gehrels, N. 2011, *ApJ*, 734, 35
 Cano, Z., Wang, S.-Q., Dai, Z.-G., & Wu, X.-F. 2017, *AdAst*, 2017, 8929054
 Cardone, V. F., Capozziello, S., & Dainotti, M. G. 2009, *MNRAS*, 400, 775
 Cardone, V. F., Dainotti, M. G., Capozziello, S., & Willingale, R. 2010, *MNRAS*, 408, 1181
 Chow, G. C. 1960, *Econometrica*, 28, 591
 Costa, E., Frontera, F., Heise, J., et al. 1997, *Natur*, 387, 783
 Dai, Z. G., & Lu, T. 1998, *A&A*, 333, L87
 Dainotti, M. G., Bernardini, M. G., Bianco, C. L., et al. 2007, *A&A*, 471, L29
 Dainotti, M. G., Cardone, V. F., & Capozziello, S. 2008, *MNRAS*, 391, L79
 Dainotti, M. G., & Del Vecchio, R. 2017, *NewAR*, 77, 23
 Dainotti, M. G., Del Vecchio, R., Shigehiro, N., & Capozziello, S. 2015, *ApJ*, 800, 31
 Dainotti, M. G., Del Vecchio, R., & Tarnopolski, M. 2018, *AdAst*, 2018, 4969503
 Dainotti, M. G., Hernandez, X., Postnikov, S., et al. 2017a, *ApJ*, 848, 88
 Dainotti, M. G., Lenart, A. L., Fraija, N., et al. 2021a, *PASJ*, 73, 970
 Dainotti, M. G., Livermore, S., Kann, D. A., et al. 2020a, *ApJL*, 905, L26
 Dainotti, M. G., Nagataki, S., Maeda, K., et al. 2017b, *A&A*, 600, A98
 Dainotti, M. G., Omodei, N., Srinivasaragavan, G. P., et al. 2021b, *ApJS*, 255, 13
 Dainotti, M. G., Petrosian, V., Singal, J., & Ostrowski, M. 2013, *ApJ*, 774, 157
 Dainotti, M. G., Postnikov, S., Hernandez, X., & Ostrowski, M. 2016, *ApJL*, 825, L20
 Dainotti, M. G., Lenart, A. L., Sarracino, G., et al. 2020b, *ApJ*, 904, 97
 Dainotti, M. G., Willingale, R., Capozziello, S., et al. 2010, *ApJL*, 722, L215
 Dall’Osso, S., Stratta, G., Guetta, D., et al. 2011, *A&A*, 526, A121
 De Pasquale, M., Oates, S. R., Racusin, J. L., et al. 2016, *MNRAS*, 455, 1027
 Della Valle, M., Chincarini, G., Panagia, N., et al. 2006, *Natur*, 444, 1050
 Dichiera, S., Troja, E., Beniamini, P., et al. 2021, *ApJL*, 911, L28
 Duncan, R. C., & Thompson, C. 1992, *ApJL*, 392, L9
 Efron, B., & Petrosian, V. 1992, *ApJ*, 399, 345
 Evans, P. A., Beardmore, A. P., Page, K. L., et al. 2009, *MNRAS*, 397, 1177
 Evans, P. A., Willingale, R., Osborne, J. P., et al. 2010, *A&A*, 519, A102
 Fraija, N., Betancourt Kamenetskaia, B., Dainotti, M. G., et al. 2021, *ApJ*, 907, 78
 Fukugita, M., Ichikawa, T., Gunn, J. E., et al. 1996, *AJ*, 111, 1748
 Fynbo, J. P. U., Watson, D., Th ne, C. C., et al. 2006, *Natur*, 444, 1047
 Gehrels, N., Ramirez-Ruiz, E., & Fox, D. B. 2009, *ARA&A*, 47, 567
 Gendre, B., Joyce, Q. T., Orange, N. B., et al. 2019, *MNRAS*, 486, 2471
 Gendre, B., Stratta, G., Atteia, J. L., et al. 2013, *ApJ*, 766, 30
 Genet, F., Daigne, F., & Mochkovitch, R. 2007, *MNRAS*, 381, 732
 Ginsburg, A., Sip cz, B. M., Brasseur, C. E., et al. 2019, *AJ*, 157, 98
 Green, G. M. 2018, *JOSS*, 3, 695
 Greiner, J., Mazzali, P. A., Kann, D. A., et al. 2015, *Natur*, 523, 189
 Heise, J., Zand, J. I., Kippen, R. M., & Woods, P. M. 2001, in *X-Ray Flashes and X-Ray Rich Gamma Ray Bursts, Gamma-ray Bursts in the Afterglow Era*, ed. E. Costa, F. Frontera, & J. Hjorth (Berlin: Springer), 16

- Hjorth, J., Sollerman, J., Møller, P., et al. 2003, *Natur*, 423, 847
- Huang, K. Y., Urata, Y., Kuo, P. H., et al. 2007, *ApJ*, 654, L25
- Kann, D. A., Klose, S., & Zeh, A. 2006, *ApJ*, 641, 993
- Kann, D. A., Klose, S., Zhang, B., et al. 2010, *ApJ*, 720, 1513
- Kann, D. A., Klose, S., Zhang, B., et al. 2011, *ApJ*, 734, 96
- Kann, D. A., Schady, P., Olivares, E. F., et al. 2018, *A&A*, 617, A122
- Kann, D. A., Schady, P., Olivares, E. F., et al. 2019, *A&A*, 624, A143
- Kelley, K., & Maxwell, S. 2003, *Psychol. Methods*, 3, 21
- Kotani, T., Kawai, N., Yanagisawa, K., et al. 2005, *NCimC*, 28, 755
- Kouveliotou, C., Meegan, C. A., Fishman, G. J., et al. 1993, *ApJ*, 413, L101
- Kumar, P., Narayan, R., & Johnson, J. L. 2008, *MNRAS*, 388, 1729
- Levan, A., Jakobsson, P., Hurkett, C., et al. 2007, *MNRAS*, 378, 1439
- Levan, A. J., Tanvir, N. R., Starling, R. L. C., et al. 2014, *ApJ*, 781, 13
- Levesque, E. M., Bloom, J. S., Butler, N. R., et al. 2010, *MNRAS*, 401, 963
- Li, L., Liang, E.-W., Tang, Q.-W., et al. 2012, *ApJ*, 758, 27
- Li, L., Wang, Y., Shao, L., et al. 2018a, *ApJS*, 234, 26
- Li, L., Wu, X.-F., Huang, Y.-F., et al. 2015, *ApJ*, 805, 13
- Li, L., Wu, X.-F., Lei, W.-H., et al. 2018b, *ApJS*, 236, 26
- Liang, E.-W., Zhang, B.-B., & Zhang, B. 2007, *ApJ*, 670, 565
- Lü, H.-J., & Zhang, B. 2014, *ApJ*, 785, 74
- Mazets, E., Golenetskii, S., Il'Inskii, V., et al. 1981, *Ap&SS*, 80, 3
- McCall, M. L. 2004, *AJ*, 128, 2144
- Metzger, B. D. 2019, *AnPhy*, 410, 167923
- Metzger, B. D., Giannios, D., Thompson, T. A., et al. 2011, *MNRAS*, 413, 2031
- Molinari, E., Vergani, S. D., Malesani, D., et al. 2007, *A&A*, 469, L13
- Narayan, R., Paczynski, B., & Piran, T. 1992, *ApJL*, 395, L83
- Norris, J. P., & Bonnell, J. T. 2006, *ApJ*, 643, 266
- Norris, J. P., Gehrels, N., & Scargle, J. D. 2010, *ApJ*, 717, 411
- Nousek, J. A., Kouveliotou, C., Grupe, D., et al. 2006, *ApJ*, 642, 389
- Oates, S. R., Page, M. J., De Pasquale, M., et al. 2012, *MNRAS*, 426, L86
- Oates, S. R., Page, M. J., Schady, P., et al. 2009, *MNRAS*, 395, 490
- O'Brien, P. T., Willingale, R., Osborne, J., et al. 2006, *ApJ*, 647, 1213
- Paczynski, B. 1998, *ApJL*, 494, L45
- Panaiteanu, A., Mészáros, P., Burrows, D., et al. 2006, *MNRAS*, 369, 2059
- Piro, L., Amati, L., Antonelli, L. A., et al. 1998, *A&A*, 331, L41
- Piro, L., Troja, E., Gendre, B., et al. 2014, *ApJL*, 790, L15
- Poole, T. S., Breeveld, A. A., Page, M. J., et al. 2008, *MNRAS*, 383, 627
- Postnikov, S., Dainotti, M. G., Hernandez, X., & Capozziello, S. 2014, *ApJ*, 783, 126
- Rastinejad, J. C., Gompertz, B. P., Levan, A. J., et al. 2022, arXiv:2204.10864
- Rea, N., Gullón, M., Pons, J. A., et al. 2015, *ApJ*, 813, 92
- Rossi, A., Rothberg, B., Palazzi, E., et al. 2022, *ApJ*, 932, 1
- Rowlinson, A., Gompertz, B. P., Dainotti, M., et al. 2014, *MNRAS*, 443, 1779
- Sakamoto, T., Hill, J., Yamazaki, R., et al. 2007, *ApJ*, 669, 1115
- Sako, S., Ohsawa, R., Takahashi, H., et al. 2018, *Proc. SPIE*, 10702, 107020J
- Schlafly, E. F., & Finkbeiner, D. P. 2011, *ApJ*, 737, 103
- Schlegel, D. J., Finkbeiner, D. P., & Davis, M. 1998, *ApJ*, 500, 525
- Si, S.-K., Qi, Y.-Q., Xue, F.-X., et al. 2018, *ApJ*, 863, 50
- Stratta, G., Dainotti, M. G., Dall'Osso, S., et al. 2018, *ApJ*, 869, 155
- Thompson, C. 1994, *MNRAS*, 270, 480
- Troja, E., Cusumano, G., O'Brien, P. T., et al. 2007, *ApJ*, 665, 599
- Usov, V. V. 1992, *Natur*, 357, 472
- van Eerten, H. 2014a, *MNRAS*, 442, 3495
- van Eerten, H. J. 2014b, *MNRAS*, 445, 2414
- van Paradijs, J., Groot, P. J., Galama, T., et al. 1997, *Natur*, 386, 686
- Vestrand, W. T., Wozniak, P. R., Wren, J. A., et al. 2005, *Natur*, 435, 178
- Virtanen, P., Gommers, R., Oliphant, T. E., et al. 2020, *NatMe*, 17, 261
- Wang, X.-G., Zhang, B., Liang, E.-W., et al. 2015, *ApJS*, 219, 9
- Wang, X.-G., Zhang, B., Liang, E.-W., et al. 2018, *ApJ*, 859, 160
- Watson, A. M., Lee, W. H., Troja, E., et al. 2016, *Proc. SPIE*, 9910, 99100G
- Willingale, R., O'Brien, P. T., Osborne, J. P., et al. 2007, *ApJ*, 662, 1093
- Woodsley, S. E. 1993, *ApJ*, 405, 273
- Woodsley, S. E., & Bloom, J. S. 2006, *ARA&A*, 44, 507
- Zaninoni, E., Bernardini, M. G., Margutti, R., et al. 2013, *A&A*, 557, A12
- Zhang, B., Fan, Y. Z., Dyks, J., et al. 2006, *ApJ*, 642, 354
- Zhang, B., & Mészáros, P. 2001, *ApJL*, 552, L35
- Zhang, B., & Meszaros, P. 2002, *ApJ*, 581, 1236
- Zhang, B., Zhang, B.-B., Virgili, F. J., et al. 2009, *ApJ*, 703, 1696
- Zhang, B. B., Liu, Z. K., Peng, Z. K., et al. 2021, *NatAs*, 5, 911